Effect of CoB Loading Amount in gC_3N_4 Nanosheet in Photocatalytic Hydrogen Generation

Mr. Chayathorn Prapaitrakool

ผลขอลปริมาณCoBที่ถูกโหลดบนgC_3N_4 nanosheetในการผลิตไฮโดรเจนจากตัวเร่งปฏิกิริยาที่ใช้แสง

นายชยธร ประไพตระกูล

วิทยานิพนธ์นี้เป็นส่วนหนึ่งของการศึกษาตามหลักสูตรปริญญาวิศวกรรมศาสตรมหาบัณฑิต
สาขาวิชาวิศวกรรมเคมี ภาควิชาวิศวกรรมเคมี
คณะวิศวกรรมศาสตร์ จุฬาลงกรณ์มหาวิทยาลัย
ปีการศึกษา 2564
ลิขสิทธิ์ของจุฬาลงกรณ์มหาวิทยาลัย

Thesis Title	Effect of CoB Loading Amount in gC_3N_4 Nanosheet in Photocatalytic Hydrogen Generation
By	Mr. Chayathorn Prapaitrakool
Field of Study	Chemical Engineering
Thesis Advisor	Professor AKAWAT SRIRISUK, Ph.D.
Thesis Co Advisor	Professor Jeffrey Chi-sheng Wu, Ph.D.

Accepted by the FACULTY OF ENGINEERING, Chulalongkorn University in Partial Fulfillment of the Requirement for the Master of Engineering

.... Dean of the FACULTY OF ENGINEERING

(Professor SUPOT TEACHAVORASINSKUN, Ph.D.)

THESIS COMMITTEE

.... Chairman

(Professor Pongtorn Charoensuppanimit, Ph.D.)

.... Thesis Advisor

(Professor AKAWAT SRIRISUK, Ph.D.)

.... Thesis Co-Advisor

(Professor Jeffrey Chi-sheng Wu, Ph.D.)

.... Examiner

(Associate Professor PATTARAPORN KIM, Ph.D.)

.... External Examiner

(Professor Okorn Mekasuwandumrong, Ph.D.)

.... External Examiner

(Associate Professor Wen-Yueh Yu, Ph.D.)

ชยธร ประไพตระกูล : ผลขอลปริมาณCoBที่ถูกโหลดบนgC$_3$N$_4$ nanosheetในการผลิต
ไฮโดรเจนจากตัวเร่งปฏิกิริยาที่ใช้แสง. (Effect of CoB Loading Amount in
gC$_3$N$_4$ Nanosheet in Photocatalytic Hydrogen Generation) อ.ที่ปรึกษาหลัก : อ.
ดร.อัครวัต ศิริสุข, อ.ที่ปรึกษาร่วม : ศ. ดร.เจฟฟรี่ ฉี-เชิง อู่

โลหะมีตระกูลราคาแพงเช่น Pt, Ru และ Ir ถูกใช้เป็นโปรโมเตอร์ของตัวเร่งปฏิกิริยา
อย่างกว้างขวางเพื่อเร่งการผลิตไฮโดรเจนด้วยตัวเร่งปฏิกิริยาที่ใช้แสงในน้ำ ในทางกลับกัน โปรโม
เตอร์ของตัวเร่งปฏิกิริยาราคาถูกอื่นๆซึ่งถูกพัฒนาสามารถเพิ่มประสิทธิภาพอัตราการผลิต
ไฮโดรเจนได้เช่นกัน เช่น โลหะฟอสไฟต์ โลหะคาร์ไบด์ และ โลหะบอไรด์ จากการศึกษาค้นคว้าที่
ผ่านมา 7wt% นิเกิลบอไรด์ (NiB) ที่บรรจุลงบนกราฟิติกคาร์บอนไนไตรด์นาโนชีท (gCNS) ได้
แสดงอัตราการผลิตไฮโดรเจนที่ดีภายใต้แสงในช่วงที่ตามองเห็น ดังนั้น งานวิจัยนี้จึงพยายามที่จะ
ตรวจสอบประสิทธิภาพในการผลิตไฮโดรเจนของโคบอลต์บอไรด์ (CoB) ในฐานะตัวช่วยเร่ง
ปฏิกิริยาบน gCNS และเปรียบเทียบกับประสิทธิภาพการผลิตไฮโดรเจนของ NiB ปริมาณของการ
โหลด CoB เปลี่ยนแปลงจาก 1-11 wt%CoB-gCNS (1-11CoB-gCNS) ปฏิกิริยาการผลิต
ไฮโดรเจนด้วยตัวเร่งจากแสงถูกดำเนินการภายใต้หลอดไฟซีนอน 300W ที่ติดตั้งตัวกรองแสงที่
มองเห็นได้ ไตรเอทาโนลามีนถูกใช้เป็นสารที่ใช้เอื้อปฏิกิริยาข้อสรุปของงานวิจัยนี้พบว่า
ประสิทธิภาพการผลิตไฮโดรเจนที่ดีที่สุดเกิดโดย 9CoB-gCNS ได้ 60.71 ไมโครโมล/กรัม/ชม.
ผลลัพธ์นี้แสดงให้เห็นการเพิ่มประสิทธิภาพการผลิตไฮโดรเจนอย่างมีนัยสำคัญ เมื่อเทียบกับ gCNS
ซึ่งเป็นผลมาจากคุณสมบัติการเดินทางของประจุที่ถูกกระตุ้นด้วยแสงที่ดีขึ้นซึ่งก็คือ การดูดกลืน
แสงที่มองเห็นได้นั้นถูกพัฒนาขึ้นอย่างมากและพลังงานช่องว่างของแถบในการดูดแสงที่มองเห็นได้
นั้นแคบลงจากการทดลองจาก UV-Vis Spectra และที่สำคัญคือ recombination rate ยังดูลง
จากการทดลอง PL และความสามารถในการเคลื่อนที่ของอีเล็กตรอนเร็วขึ้นเป็นอย่างมากจากการ
ทดลอง EIS ซึ่งปัจจัยเหล่านี้เป็นเหตุผลหลักของความสามารถในการผลิตไฮโดรเจนที่ดีที่สุดของ
9CoB-gCNS ยิ่งไปกว่านั้น ความสามารถการผลิตไฮโดรเจนของ9CoB-gCNS ยังคงมากกว่ากว่า
7NiB-gCNS (51.29 ไมโครโมล/กรัม/ชม.)

สาขาวิชา	วิศวกรรมเคมี	ลายมือชื่อนิสิต ....
ปีการศึกษา	2564	ลายมือชื่อ อ.ที่ปรึกษาหลัก ....
		ลายมือชื่อ อ.ที่ปรึกษาร่วม ....

6370350621 : MAJOR CHEMICAL ENGINEERING

KEYWORD: Cobalt Boride, Graphitic Carbon Nitride Nanosheet, Photocatalyst, Photocatalytic Hydrogen Generation

Chayathorn Prapaitrakool : Effect of CoB Loading Amount in gC_3N_4 Nanosheet in Photocatalytic Hydrogen Generation. Advisor: Prof. AKAWAT SRIRISUK, Ph.D. Co-advisor: Prof. Jeffrey Chi-sheng Wu, Ph.D.

Noble metals, such as Pt, Ru, and Ir, have been widely used as expensive catalyst promoters to enhance the photocatalytic hydrogen evolution reaction (HER). In contrast, other cheaper catalyst promoters that can also promote high HER performance have been developed, such as metal phosphides, and metal borides. Recently, nickel boride (NiB) loaded on graphitic carbon nitride nanosheet (gCNS) has exhibited promising HER performance under visible light. Thus, this research attempted to investigate HER performance of cobalt boride (CoB) as a cocatalyst on gCNS and compare to the HER performance of NiB. The amount of CoB loading was varied from 1-11 wt%CoB-gCNS (1-11CoB-gCNS). The reaction was carried out under 300W Xenon lamp equipped with visible light filter. Triethanolamine was employed as a sacrificial agent. The best HER performance was observed for 9CoB-gCNS at 60.71 µmole/g/h of H_2 evolved. This result showed a significant enhancement in HER performance, compared with that of pure gCNS, which was attributed to better photoelectrochemical properties of the photocatalyst. The light absorbance and band gap energy (from UV-Vis spectra) of 9CoB-gCNS were significantly enhanced. Additionally, the recombination rate from PL and mobility of electron from EIS were lower which support the superior HER performance of 9CoB-gCNS which was better than that of 7NiB-gCNS (51.29 µmole/g/h).

Field of Study:	Chemical Engineering	Student's Signature	....
Academic Year:	2021	Advisor's Signature	....
		Co-advisor's Signature	....

ACKNOWLEDGEMENTS

TABLE OF CONTENTS

Page

LIST OF TABLES

LIST OF FIGURES

Chapter 1
Introduction

1.1. Rationale

The global warming situation has become one of the greatest challenges in modern age. One significant contribution to the situation is carbon dioxide (CO_2) emission from combustion of fossil fuel, which stimulates the greenhouse effect [1]. In order to relieve this problem, scientists have researched many solutions to replace fossil fuel with clean renewable energy. Hydrogen has been contemplated as the high potential clean energy which could replace fossil fuel in the future [2]. Generally, hydrogen must be produced from other compounds containing hydrogen atoms, for instance fossil fuel, nuclear, and renewable energy source [3]. The idealistic goal of hydrogen production is to minimize cost and emission level as low as possible.

Hydrogen can be produced by many alternative processes, such as steam reforming, coal gasification, thermochemical and biological processes of biomass [4]. Though hydrogen is considered as a clean energy source in a general aspect, these production processes would emit significant amount of greenhouse gas. Hence, the byproducts and the required resources in the production of hydrogen are the two important factors which have to be carefully considered in order to obtain the completely clean product and process. Other alternative processes to produce hydrogen are to utilize hydropower, wind energy, or solar energy for the reaction. The solar energy is chosen in this research as it has fewer geography limitations.

Photocatalytic water splitting reaction to generate hydrogen and oxygen is the process that is from fossil fuels and has zero carbon dioxide emission [5]. This process has a number advantages, including reasonable solar-to-hydrogen efficiency, low-cost production, high potential to separately obtain hydrogen and oxygen from the reaction, and acceptable size of reactor for household applications [4].

Semiconductors has been researched as the photocatalytic material for the photocatalytic water splitting reaction since 1972 by Fujishima and Honda [6]. After a few decades later, a lot of semiconductors, for instance TiO_2 [7], ZnO [8], SnO_2 [9],

Fe_2O_3 [10], CdS [11], $BiVO_4$ [12], and Cu_2O [13], have been considered as highly efficient photocatalysts under UV or visible light. In the photocatalyst, valence band (VB) and conduction band (CB) theoretically exist which VB locates in the lower energy level, comparing to CB, and the difference between those bands is band gap energy [14]. Theoretically, three fundamental steps are included in the water splitting process. Firstly, the photocatalyst absorbs photon, which has greater energy than its band gap, and electrons (e^-) in a VB are excited to a CB, which leaves holes (h^+) in the VB. Secondly, the oxidation of water is occurred by h^+ to produce O_2 and proton (H^+). Then the reduction of H^+ by e^- in the CB generates H_2 [15].

Graphitic Carbon Nitride (gCN) is a metal free polymeric p-type semiconductor, which is made of Earth abundant elements (including carbon and nitrogen). The structure of gCN resembles to that of graphene. gCN possesses 2.7 eV of band gap energy and its color is yellow, resulting in the capability to absorb light around 460 nm [16]. Not only do gCN illustrates a suitable band gap for water splitting reaction, but it also has high chemical and photo stabilities. Despite its advantages, high recombination rate of photogeneration of electron and hole pairs can be observed during the photocatalytic water splitting reaction, causing low efficiency of hydrogen generation [17]. Furthermore, because of over-energized band gap of gCN comparing to potential of water (1.23 eV), gCN can be only activated in blue-light up to 450 nm (the minority wavelength of visible light) [18]. For the past decades, some techniques, such as doping, copolymerization, and dye sensitization, have been utilized in order to refine the efficiency of gCN for photocatalytic water splitting reaction under the visible light. For example, doping Platinum as the noble metal to gCN can drastically increase hydrogen evolution rate (HER) from around 1 $\mu molh^{-1}$ to 12 $\mu molh^{-1}$ [19]. However, noble metal is not the ideal material for doping method due to their high cost and rarity. As a result, doping gCN with a cheap promoter, for instance metal phosphide, metal sulfide, and metal carbide, is more desirable. Metal boride is one of the economical cocatalyst that do not receive enough attention. Nickel boride (NiB) has been applied as a dopant of gCN and successfully shows the enhancement of HER performance in the photocatalytic hydrogen generation under visible light source [20].

In this research, due to the economic cost of metal boride and promising HER rate result of NiB doped on graphitic carbon nitride nanosheet (gCNS), research on metal boride continues with the substitution of NiB with cobalt boride (CoB) as the cocatalyst on gCNS photocatalyst. gCNS in this research was synthesized by a one-step exfoliation method using nitrogen-rich precursor to obtain gCNS with high surface area and active site for photocatalysis. For cocatalyst loading method, different wt% from 1 to 11 of CoB were doped on CNS by an impregnation-reduction method to observe which wt% demonstrates the highest HER in the photocatalytic hydrogen generation reaction. In addition, 7 samples of CoB-CNS from Slovenia's laboratory with a different exfoliation technique (probe-type exfoliation) are provided to compare the efficiency of HER with CoB-CNS in this research. These samples from Slovenia will be used as a reference as a confirmation of HER performance of CoB loaded gCNS that both batches of samples will show similar result. Additionally, 7 wt% NiB loaded on gCNS was synthesized as a reference and compared with CoB-gCNS which possesses the highest HER performance.

1.2. Objective

To investigate effect of different weight% of CoB on gCNS to the photocatalytic hydrogen generation under visible light and compare the result with hydrogen generation from NiB loading on gCNS.

1.3. Research Scope

1.3.1. Photocatalyst Preparation

1.3.1.1.   CoB-gCNS from this research

Six different wt% (1 to 11 wt%) of CoB loaded on gCNS are synthesized starting with a one-step exfoliation of melamine to obtain gCNS following by loading different wt% of CoB on gCNS with an impregnation-reduction method.

1.3.1.2.   CoB-gCNS from Slovenia's laboratory

Five different wt% (0 to 7 wt%) of CoB loaded on gCNS and 7NiB-gCNS were synthesized beginning with thermal condensation of melamine following by probe-

type exfoliation to obtain gCNS. Then, impregnation-reduction is conducted to load CoB with different amount CNS to produce 6 variations of CoB-gCNS samples.

1.3.1.3.   7NiB-gCNS

7wt% NiB loaded on gCNS is synthesized with the same step as the reference sample for photocatalytic hydrogen generation reaction because of the successful HER rate result from the previous research [20].

1.3.2.   Photocatalytic Hydrogen Generation Reaction

The reaction is conducted for 4 h in 310 ml Pyrex glass reactor and the HER performance were collected for every 30 min. After the reaction is finished, the photocatalyst sample is recycled to be used in the photocatalytic hydrogen generation reaction again. In addition, the visible light source which activates the reaction is from a 300W Xe lamp.

1.3.3.   Characterization

After all the photocatalyst samples are ready, they are characterized by 8 techniques listed below.

1. X-Ray Diffraction (XRD): Observing the microstructure and phase
2. Scanning electron microscopy (SEM): Observing the morphology
3. X-Ray Photoelectron Spectroscopy (XPS): Revealing the surface chemical states
4. UV-vis Spectrophotometer (UV-vis): Determining Light adsorption range
5. Photoluminescence (PL): Observing the behavior of electron and hole (recombination rate)
6. BET surface area measured by N_2 adsorption: Determining specific Surface Area (SSA)
7. Energy Dispersive X-ray spectroscopy (EDX): Determining the composition of the samples
8. Electrochemical Impedance Spectroscopy (EIS): Observing electron mobility

1.4. Research Methodology

```
                        ┌─────────────────────────┐
                        │     CoB-CNS Synthesis    │
                        └─────────────────────────┘
```

CoB-CNS Synthesis

Slovenia Laboratory

This research

gCNS Preparation

Bulk gCN is prepared by thermal condensation of melamine and CNS is synthesized by probe-type ultrasonicating bulk gCN

gCNS Preparation

gCNS is synthesized by grinding melamine with NH_4Cl and heated.

CoB Impregnation-Reduction

CoB 1, 3, 5, and 7 wt% are loaded by impregnation-reduction method.

CoB Impregnation-Reduction

CoB 1, 3, 5, 7, 9, and 11 wt% are loaded by impregnation-reduction method.

Photocatalytic Water Splitting Reaction

HER rates of all samples are determined by 6 h photocatalytic water splitting reaction under visible light from 300W Xe lamp

Photocatalyst Characterization
- XRD
- SEM-EDX
- XPS
- UV-vis
- PL Intensity
- N_2 Adsorption
- EIS

Discussion & Conclusion

1.5. Project Timeline

Steps	Activity	2021							2022					
		6	7	8	9	10	11	12	1	2	3	4	5	6
1	Literature review	█	█	█	█	█	█	█	█	█	█	█	█	
2	Practice to synthesize gCNS					█		█		█	█			
3	Learn to set up and conduct the photocatalytic water splitting reaction					█								
4	Conduct the photocatalytic water splitting reaction of all samples from Slovenia's lab for HER rate result						█	█						
5	Preparation of calibration curve of H_2 for GC						█			█				
6	Preparation of CoB-gCNS									█	█	█	█	
7	Preparation of 7NiB-gCNS									█	█	█	█	
8	Conduct the photocatalytic water splitting reaction synthesized samples									█	█	█	█	
9	Characterization of samples									█	█	█	█	
10	Writing thesis report												█	█

Chapter 2

Theory

2.1. Photocatalytic Water Splitting reaction

    Originally, photocatalytic water splitting reaction is the mimic version of the natural photosynthesis. Photosynthesis of plants use natural light to activate the reaction between absorbed CO_2 and water to produce glucose and O_2 [21]. In contrast, photocatalytic water splitting reaction uses artificial light to activate the reaction of photocatalyst (semiconductor) and water in a reactor to produce H_2 and O_2. A semiconductor consists of valence band (VB) and conduction band (CB). Energy difference between these two levels is said to be the band gap (E_g). Without excitation, both the electrons (e^-) and holes (h^+) are in valence band. The whole process of traditional photocatalytic water splitting reaction is illustrated in Figure 2-1. To begin with the first step, the photocatalyst in water absorbs light, which has higher energy than its band gap, to excite electrons (e^-) in a valence band (VB) to a conduction band (CB) which leaves holes (h^+) in the VB. For the following step, the oxidation of water is occurred by h^+ to produce O_2 and proton (H^+). Lastly, the reduction of H^+ by e^- in the CB generates H_2. The equations of the photocatalytic water splitting are shown in Eq. 2.1 to Eq 2.4 [22].
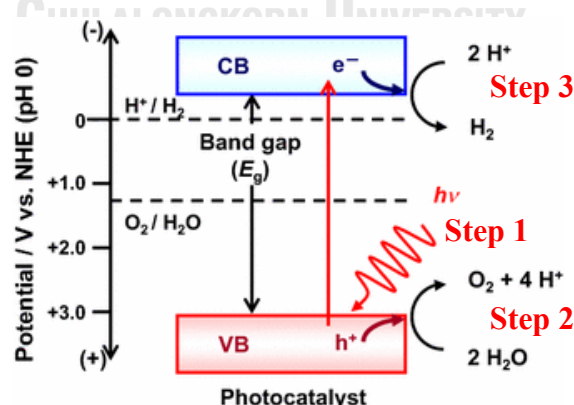
Figure 2-1 Process of photocatalytic water splitting reaction [23]

Photoexcitation: Photocatalyst + hv ➜ Photocatalyst + e⁻ + h⁺ (Eq 2.1)

Reduction: 4H⁺ + 4e⁻ ➜ 2H₂ $\qquad E^0_{H^+/H_2} = 0.00\ V$ (Eq 2.2)

Oxidation: 2H₂O + 4h⁺ ➜ 4H⁺ + O₂ $\qquad E^0_{O_2/H_2O} = +1.23\ V$ (Eq 2.3)

Overall reaction: 2H₂O ➜ 2H₂ + O₂ $\qquad E^0_{O_2/H_2O} = +1.23\ V$ (Eq 2.4)
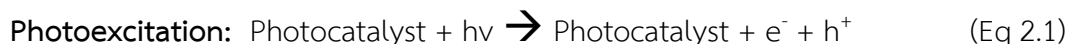
The photocatalytic water splitting reaction is considered as an endothermic reaction and nonspontaneous reaction due to high positive Gibb's energy (+237.13 kJ/ml) [22]. In order to proceed this reaction, VB and CB of the applied semiconductor have to be more positive and negative, respectively, than the redox potential of water which means VB location has to be more than +1.23 eV and CB location has to be lower than 0.00 eV as shown in Figure 2-1.

2.2. Graphitic carbon nitride (gCN)

gCN is a 2D semiconductor sheets formation of heptazines (tri-s-triazines) and each heptazine is interconnected to neighbor of itself via tertiary amines (as shown in Figure 2-2) [24]. Between the stack layer of gCN, Van der Waal forces connect sheets of gCN together, which enhancing the stability of gCN in most solvents [18]. Intrinsically, gCN approximately possesses band gap energy of 2.7 eV (as shown in Figure 2-3), conduction band (CB) and valence band (VB) position are -1.1 eV and +1.6 eV, respectively [18]. In addition, gCN monolayer structure is resemble to graphene ,which means the surface area of gCN can theoretically be almost 2500 m²g⁻¹ [18]. In Table 2-1, the chemical and physical properties of gCN are demonstrated.
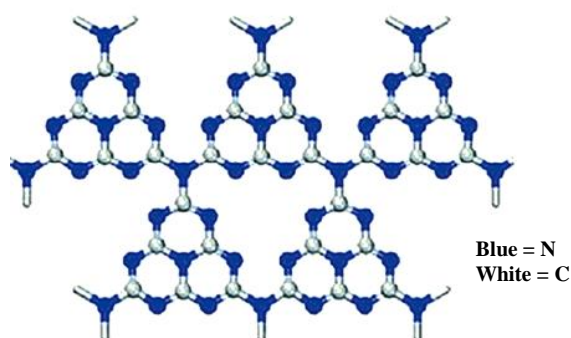
Figure 2-2 gCN monolayer (tri-s-triazines structure) [25]
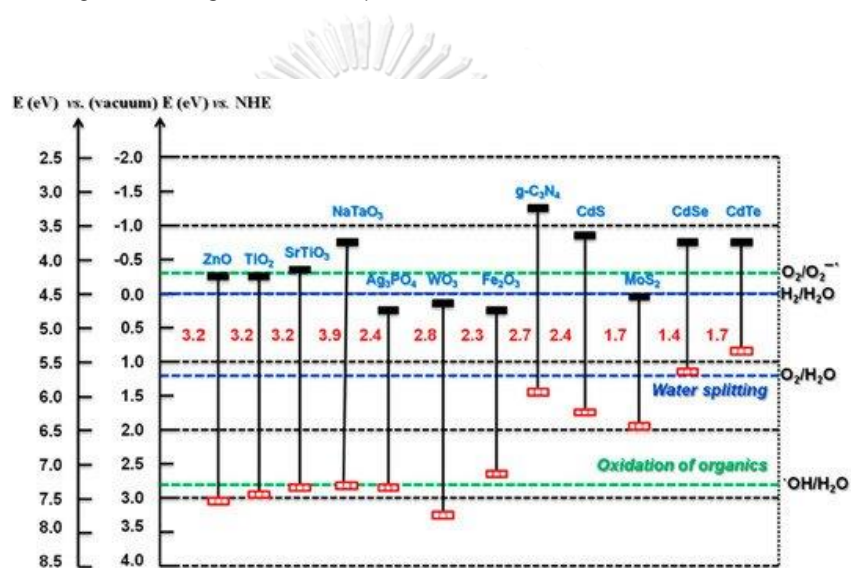
Figure 2-3 Band gap energy of gCN and other semiconductors [26]

Table 2-1 Properties of gCN

Properties

Appearance	Off-white to yellowish-brown powder
Density	2.336 g/cm^3
Temperature stability	Up to 650°C in inert atmosphere
Thermal conductivity	1.25 W/m·K
Average particle size	0.076-0.137 μm
Specific surface area	>35 m^2/g

Generally, N_2-rich precursors, for instance melamine, urea, dicyandiamide, and cyanamide, are used to synthesize gCN by the thermal condensation [18]. Each N_2-rich precursor provides different properties of gCN, such as, band gap energy, and surface area [18]. Table 2-2 shows the properties of gCN from different types of N_2-rich precursors.

Table 2-2 Band gap energy and surface area of gCN from different precursors [18]

Precursor	Reaction temperature, time and atmosphere	Band gap [eV]	Surface area [$m^2\ g^{-1}$]
Cyanamide	550 °C, 4 h, air	2.70	ca. 10
Melamine	500 °C, 2 h, air	2.80	ca. 8
	580 °C, 2 h, air	2.75	
Dicyandiamide	550 °C, 2 h, air	2.75	ca. 10
Thiourea	450 °C, 2 h, air	2.71	ca. 11
	550 °C	2.58	ca. 18
	650 °C	2.76	ca. 52
Urea	550 °C, 0 h, air	2.72	ca. 31
	550 °C	2.68	ca. 62
	550 °C	2.72	ca. 75
	550 °C	2.78	ca. 288

The result from the fabrication is bulk gCN which is the stack formation of gCN sheets. However, bulk gCN still has relatively low surface area due to the dense stack formation. Hence, the exfoliation of bulk gCN to gCNS (Figure 2-4), and gCN nanoflakes is also required. In other words, gCNS can be obtained by destroying these weak forces between layers of bulk gCN. Not only does the surface area of CNS drastically increases, but the diffusion length of charge carriers also decreases in both vertical and horizontal direction of the gCN layers [27].
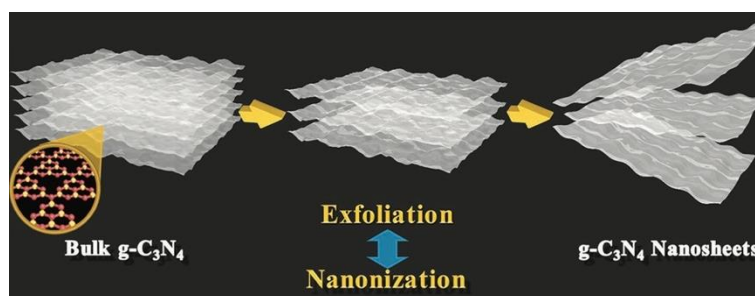
Figure 2-4 The transformation of bulk gCN to gCNS [28]

2.2.1. Exfoliation of bulk gCN

The exfoliation method of bulk gCN does matter to the properties of gCNS. Some well-known exfoliation techniques including thermal exfoliation, chemical treatment, and ultrasonication exfoliation, have been applied to provide gCNS. For thermal exfoliation, bulk gCN is simply heat in at $500^{\circ}C$ in the furnace in an ambient environment for a certain period [29]. This technique uses heat to brake weak forces between stack layer of bulk gCN. This method is relatively easy to implement comparing with other methods. For chemical exfoliation, acid solution can be applied to exfoliated bulk gCN. For example, concentrated H_2SO_4 solution intercalates between layers of bulk gCN to generate gCNS [18]. On the other hand, ultrasonication exfoliation is proceeded by mix bulk gCN with the solvent, such as solvent of ethanol and DI water, following by sonicating for 10 h to produce gCNS [29]. Additionally, one-step exfoliation is quite simple and less time consumed technique. The proportion of NH_4Cl is added to the N_2-rich precursor following by conducting the thermal condensation of the mixture. During the heating, NH_3 and HCl gases are continuously released from the mixture which can optimize heat transfer of the reaction and also perform as a bubble template for high porosity structure of the final product [30].

Nevertheless, gCNS still cannot facilitate photocatalytic water splitting reaction to generate H_2 because of the lack of H^+ reduction active site and high recombination rate of excited electron in CB in gCNS [17]. Moreover, the adsorption range of gCNS (up to 460 μm) is not ideal for visible light from the sun light (up to 740 μm) [17].

The efficiencies of other exfoliation techniques, including ultrasonic exfoliation, and one-step exfoliation, are compared with chemical and thermal exfoliation. For one-step exfoliation, the N_2-rich precursor (urea) dissolved in DI water is heated in at $550^{\circ}C$ for 3 h to obtain the final sample. In addition, in this research, bulk gCN is stirred with concentrated H_2SO_4 for 8 h for chemical exfoliation; bulk gCN is heated for 2 h at $500^{\circ}C$ for thermal exfoliation; and bulk gCN is sonicated for 10 h for ultrasonic exfoliation. Surface area, pore volume, and interlayer distance of

photocatalyst from thermal (UHCN), chemical (UACN), ultrasonic (USCN), and one-step (UWCN) exfoliation are compared with bulk gCN (UCN) in Table 2-3. It is clear that UWCN provide the best result because during the heat process, the rapid vaporization of DI water and etching NH_3 are occurred influencing in high porous structure [29]. The high porous structure provides more active sites in the samples and shortens the diffusion length of the charge which reduce the chance of rapid recombination [29].

Table 2-3 Surface area, pore volume, and interlayer distance of all synthesized sample [29]

Samples	Surface area (m^2/g)	Pore volume (cm^3/g)	Interlayer distance (nm) [a]
UCN	44.91	0.497	0.328
UHCN	72.14	0.616	0.324
UACN	16.45	0.242	0.323
USCN	69.73	0.592	0.326
UWCN	146.62	0.908	0.328

2.3. Metal-doping gCNS

Metal doping is one of the methods that can enhance the photocatalytic activity of the photocatalyst such as improving the carrier mobility, shortening band gap, decreasing the recombination rate, and increasing the light adsorption [18]. Due to the existence of nitrogen atoms which has negative charge in gCNS, it can interact with cation of doped metal to form a bond. Some metals, for instance Fe^{3+}, Mn^{3+}, Co^{2+}, Ni^{2+}, and Cu^{2+}, have been proved as the effective material to refine the photocatalytic activity of CNS [18]. Figure 2-5 shows the scheme of electron transfer in metal doped photocatalyst. From the theory, Femi level of metal is lower than CB of a photocatalyst causing excited electrons in CB transfer to doped metal facilitating the separation between hole and electron resulting in decline of recombination rate [31]. Then, electrons in doped metal will proceed the reduction reaction to generate H_2.
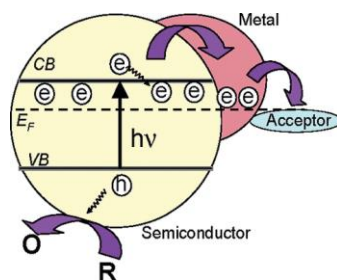
Figure 2-5 The transfer of electrons in a metal doped photocatalyst [31]

2.3.1. Transition Metal Borides (TMBs) Cocatalyst

Comparing TMBs to noble metals, such as Pt, Ru, Ir, and Pd, TMBs are totally more economical because of their considerable quantity [32]. Ease of synthesis is also counted as its benefit since TMBs can be fabricated by simple method like chemical reduction which is carried out to deposit TMBs on the substrates surface. This synthesis method is low energy consumption process, nontoxicity, and easy for upscaling the production. More importantly, TMB's row on the photocatalytic water splitting are quite spectacular. Table 2-4 shows the result of the photocatalytic activity from TMBs as cocatalyst on different substrates.

In the past, TMBs have been applied as a cocatalyst for the replacement of noble metal such as Pt. In one particular research, CoB, NiB, and FeB (fabricated by a simple chemical reduction) are used as the cocatalyst to load on the substrate (CdS) to observe the activity of HER rate from the photocatalytic water splitting reaction under the visible light [33]. According to Figure 2-6, CoB loaded on CdS shows the highest HER rate which is also higher than 1%wt Pt loaded on CdS (synthesized by mixing CdS with chloroplatinic acid hexahydrate).

Figure 2-6 Hydrogen generation rate of metal borides and Pt loaded on CdS [33]

Table 2-4 Metal borides doped photocatalyst activity [32]

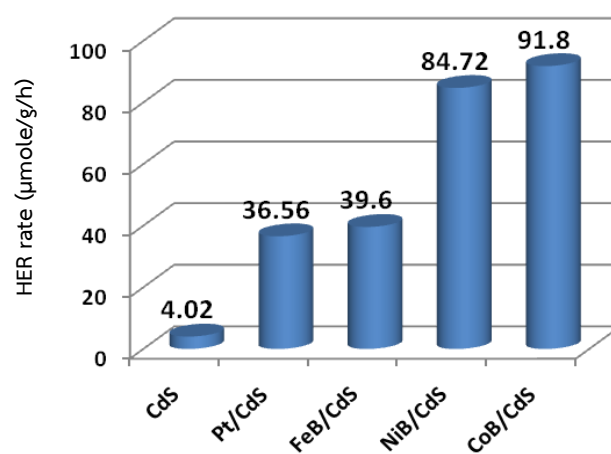| Catalyst	Substrate used	Electrolyte	Loading amount [mg cm^{-2}]	Overpotential [mV]		Tafel slope [mV dec^{-1}]		Stability and recyclability		Structure
				HER	OER	HER	OER	HER	OER	
Mo–B[25]	Carbon paste	1 M H$_2$SO$_4$	2.50	≈225 (20 mA cm^{-2})	–	55	–	48 h	–	Crystalline
		1 M KOH	2.30	≈240 (20 mA cm^{-2})	–	59	–	48 h	–	
Co–P–B/rGO[54]	GC	0.1 M PBS	0.28	639 (10 mA cm^{-2})	400 (10 mA cm^{-2})	82	68	2.7 h	2.7 h	Partially crystalline
Co–B pellet[26]	None	0.5 M KPi	–	251 (10 mA cm^{-2})	–	75	–	40 h, 1000 cycles	–	Amorphous
Ni–B[27]	GC	1 M HClO$_4$	1.00	132 (20 mA cm^{-2})	–	53, 112	–	8 h	–	Amorphous
		1 M KOH		194 (20 mA cm^{-2})	–	–	–	8 h	–	
Co$_2$B[28]	GC	0.1 M KOH	0.21	328 (10 mA cm^{-2})	380 (10 mA cm^{-2})	136.2, 177	45	–	60 h, 5000 cycles	Crystalline
Co–Ni–B[47]	GC	0.5 M KPi	2.10	170 (10 mA cm^{-2})	–	51	–	45 h, 1000 cycles	–	Amorphous
		1 M NaOH		133 (10 mA cm^{-2})	–	121	–	45 h, 1000 cycles	–	
Co–B[47]	GC	0.5 M KPi	2.10	197 (10 mA cm^{-2})	–	71	–	–	–	Amorphous
		1 M NaOH		166 (10 mA cm^{-2})	–	–	–	–	–	
NiB$_x$ film[29]	Cu foil	0.5 M H$_2$SO$_4$	1.40	45 (10 mA cm^{-2})	–	43	–	42 h	–	Amorphous
		1 M PBS		54 (10 mA cm^{-2})	–	77	–	20 h, 2000 cycles	–	
		1 M KOH		135 (10 mA cm^{-2})	–	88	–	20 h	–	
Ni–B[85]	Ni foam	1 M KOH	12.30	125 (20 mA cm^{-2})	360 (100 mA cm^{-2})	93	76	10 h	10 h	Amorphous
MoB$_2$[30]	Carbon sheet	0.5 M H$_2$SO$_4$	0.20–0.30	230 (2.5 mA cm^{-2})	–	75	–	1000 cycles	–	Crystalline
Co$_2$B–CoSe$_2$[108]	GC	1 M KOH	0.40	300 (10 mA cm^{-2})	320 (10 mA cm^{-2})	76	56	30 h	–	Amorphous
Co–B–NCNT[98]	GC	0.1 M KOH	0.21	–	370 (10 mA cm^{-2})	–	–	–	51 h	Crystalline
Co–Mo–B[50]	GC	0.5 M KPi	2.10	96 (10 mA cm^{-2})	–	56	–	40 h, 5000 cycles	–	Nanocrystalline
		1 M NaOH		66 (10 mA cm^{-2})	320 (10 mA cm^{-2})	67	155	40 h, 5000 cycles	10 h, 1000 cycles	
Co–Ni–B[51]	Ni foam	KOH	–	205 (10 mA cm^{-2})	313 (10 mA cm^{-2})	–	120	12 h	12 h	Partially crystalline
Co–W–B[52]	Ni foam	1 M KOH	–	98 (10 mA cm^{-2})	360 (10 mA cm^{-2})	83	–	12 h	–	Nanocrystalline
Co–B[139]	Carbon paper	1 M KOH	2.56	–	340 (10 mA cm^{-2})	–	63			Crystalline
Co$_2$B[139]				109 (10 mA cm^{-2})	287 (10 mA cm^{-2})	–	50.7	–	12 h, 1000 cycles	Crystalline
Co$_3$B[139]				–	312 (10 mA cm^{-2})	–	53	–	–	Crystalline
Co–B[139]	GC	0.1 M KOH	0.20	–	405 (10 mA cm^{-2})	–	–	–	–	–
Co$_2$B[139]				–	371 (10 mA cm^{-2})	–	–	–	–	–
Co$_3$B[139]				–	378 (10 mA cm^{-2})	–	–	–	–	–
Co–Fe–B[76]	Cu sheet	1 M KOH	1.20	–	298 (10 mA cm^{-2})	–	62.6	–	12 h	Amorphous
Etched Mo–Al–B[137]	Unsupported	0.5 M H$_2$SO$_4$	–	361 (10 mA cm^{-2})	–	–	–	24 h	–	Crystalline

Additionally, the research about NiB as a TMB cocatalyst loaded on gCNS photocatalyst by simple chemical reduction to determine the most appropriate percentage of NiB on gCNS for HER rate from photocatalytic water splitting reaction was conducted [20]. It was found that 7.5 wt% NiB loaded on gCNS can produce the highest HER rate as shown in Figure 2-7. The excess amount of NiB loading can cause the coverage of active sites on gCNS leading to shape decrease of HER rate [20]. In Figure 2-8A, blue line (d) is the absorbance of 7.5 wt% NiB-gCNS which is higher than other samples at around 450 to 800 nm. From Figure 2-8B, lower recombination rate can be observed on 7.5 wt% NiB-gCNS because of lower PL intensity comparing to gCNS.
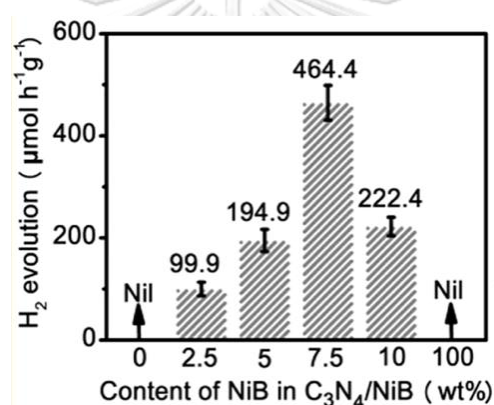

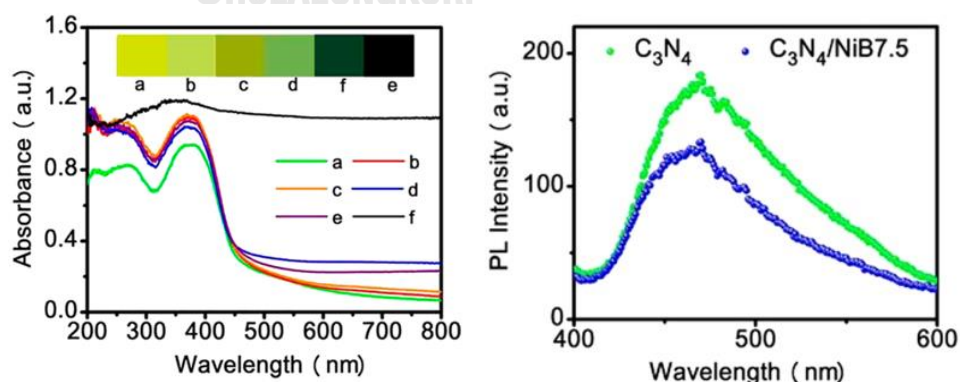**Figure 2-7** Hydrogen generation rate of NiB-gCNS samples [20]

Figure 2-8 (A) UV-vis spectra, (B) Photo Luminescence Intensity [20]

2.3.2. Cobalt Boride (CoB)

Amorphous Cobalt Boride (CoB) is one of the low-cost transition metal borides (TMBs) which can be used as a cocatalyst. It is usually synthesized from sodium borohydride ($NaBH_4$) and cobalt chloride hexahydrate ($CoCl_2.6H_2O$). Generally, CoB exhibits high porosity, high chemical stability. Focusing on the electrochemical properties, CoB possesses d-electronic configuration which provides various oxidation states resulting in introduction of new d-band center electrons transportation. Furthermore, due to the strong hybridization of d-state and p-state of CoB, covalent bond between cobalt and boride is strong and shows well electrocatalytic activity and electron transfer from boron to vacant d-orbital of cobalt makes CoB even more active [34]. Generally, in amorphous CoB, because of the electronegativity value of B (2.01) is higher than Co (1.70), electrons will transfer from Co to B which leaves Co site to be electron deficient. However, the partial reverse electron transfer toward Co is observed in amorphous CoB when it is stimulated which refills Co d-band orbital to become active site for HER as shown in Figure 2-9 [32]. Additionally, properties of amorphous CoB are shown in Table 2-5.

Table 2-5 Properties of amorphous CoB [35]

Properties

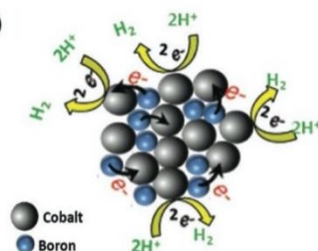| Appearance	Black Powder
Density	7.25 g/cm^3
Molecular Weight	69.744
Melting Point	1460°C
Average particle size	18-22 nm

Figure 2-9 The partial transfer of electrons from B back to Co in amorphous CoB [32]

There is a research about loading CoB on gCNS by an electrostatic self-assembly coupled calcination method. The synthesized CoB is mixed with gCNS in DI water for 8 h following by 2 h calcination [36]. The researcher introduced the heterojunction of CoB loaded on gCNS in Figure 2-11. The Figure 2-10 shows that bonding between Co atom (red) and N atom (blue) is formed. From the DFT calculation in this research paper, the work function (vs vacuum level) of CoB, gCNS, and CoB-gCNS are obtained. After the contact of CoB and gCNS, the different in work function facilitates the movement of electron from upward bending of gCNS to CoB (via Co-N bond transfer channel) as shown in Figure 2-11. This action enhances the separation of electrons and holes which reduce the recombination rate.
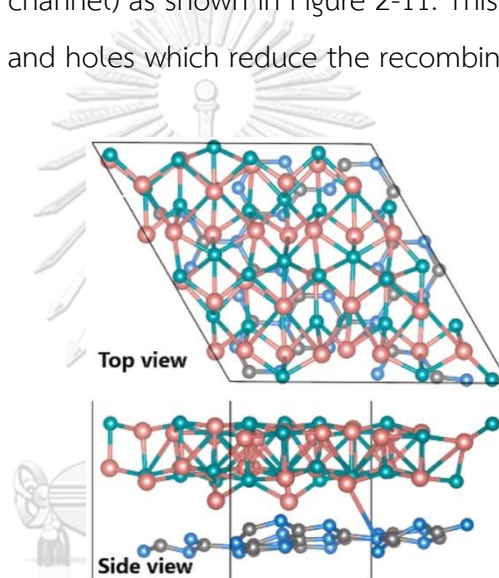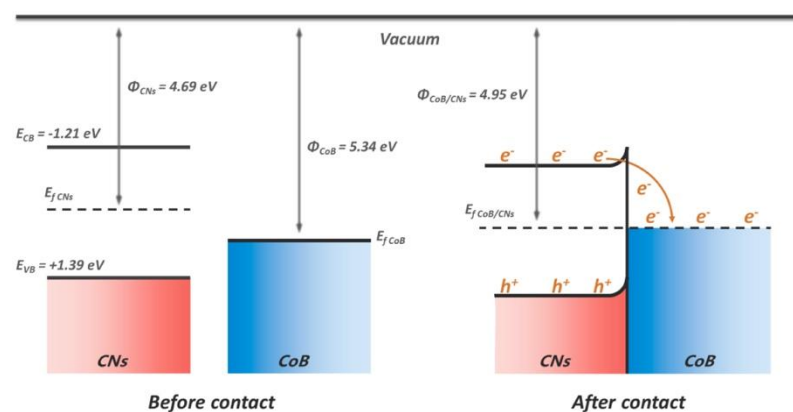

Figure 2-10 CoB-gCNS structure [36]

Figure 2-11 Work function vs vacuum level of CoB-gCNS [36]

2.4. Sacrificial Agent (electron doner/hole scavenger) for gCN

Sacrificial Agent is usually added to the solution for the photocatalytic water splitting reaction to enhance the production of H_2. The role of the sacrificial agent is to scavenge the photogenerated holes in the valence band (VB) of the photocatalyst reducing the recombination rate [37]. Moreover, backward reaction is less likely to occur because the generated O_2 from the oxidation on the VB is greatly reduced leading to more H_2 yield on the conduction band [37].

In general, methanol has been frequently applied as an organic sacrificial agent in the photocatalytic reaction and the mechanism is shown in Figure 2-12. From Figure 2-12, methanol will consume photogenerated hole in the valence band to form $°CH_2OH$ and H^+ in step (3). Then, $°CH_2OH$ can donate electron directly to the active site of the photocatalyst and producing HCHO and H^+ in step (4).
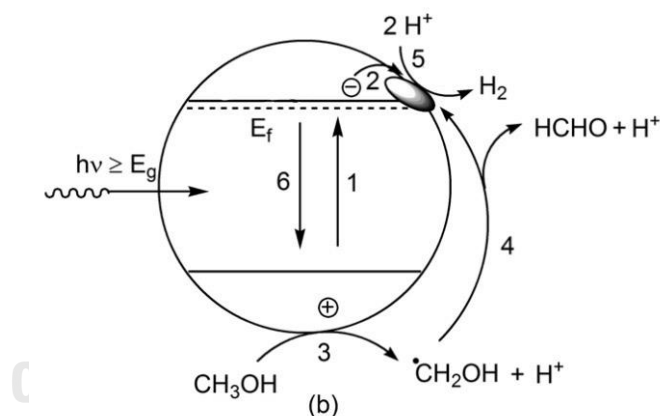
Figure 2-12 Mechanism of methanol as sacrificial agent [37]

It has been shown that triethanolamine (TEOA) is the most suitable sacrificial agent for gCN to enhance the HER rate during photocatalytic water splitting reaction. Figure 2-13 reveals the HER rate from the different sacrificial reagents which TEOA obviously provides the best rate among others. The possible reason behind this is TEOA can effectively attach on the amine-rich gCN surface and ensure the degradation of Pi conjugated in gCN structure and photo corrosion [38]. TEOA also improves the interaction between water molecules and gCN (low hydrophilicity)

surface by acting as a binding ligand and also efficiently consumes photogenerated holes which is oxidation of TEOA (as shown in Figure 2-14) in VB producing H+. At the moment, TEOA is degraded and converted to TEOA+. In addition, the hole consumption by TEOA also reduces the recombination rate [39].

Figure 2-13 Result of HER rate from different sacrificial agent with gCN [38]

Figure 2-14 Mechanism of photocatalytic hydrogen generation with TEOA [40]

Chapter 3
Experimental detail

3.1. Material and Chemical

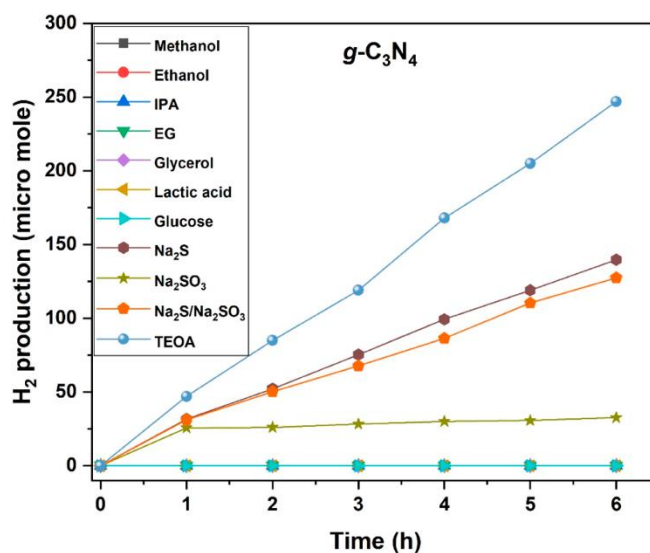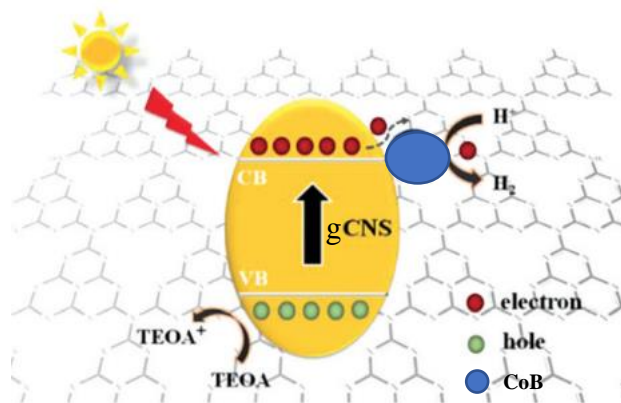Chemical powder and solution used in this research and Slovenia's lab are shown in table Table 3-1 and Table 3-2, respectively.

Table 3-1 The required chemicals for the photocatalyst samples synthesis in this

Name	Chemical Formula	Supplier
Melamine	$C_3H_6N_6$	Alfa Aesar
Ammonium Chloride	NH_4Cl	SIGMA-ALDRICH
Sodium Borohydride	$NaBH_4$	ALDRICH
Cobalt (II) Chloride Hexahydrate	$CoCl_2.6H_2O$	SIGMA-ALDRICH
Nickel (II) nitrate hexahydrate	$Ni(NO_3)_2.6H_2O$	Alfa Aesar
Triethanolamine (TEOA)	$C_6H_{15}NO_3$	SIGMA-ALDRICH

research

Table 3-2 List of chemicals for CoB-gCNS synthesis from Slovenia's laboratory

Name	Chemical Formula	Supplier
Melamine	$C_3H_6N_6$	SIGMA-ALDRICH
Sodium Borohydride	$NaBH_4$	Fluka Analaytical
Cobalt (II) nitrate Hexahydrate	$Co(NO_3)_2.6H_2O$	Alfa Aesar

3.2. The preparation of photocatalyst

3.2.1. CoB-gCNS samples in this research

The mixture at a ratio of 1 to 5 of melamine used as the N_2-rich precursor and NH_4Cl, was grinded until a homogenous white powder was obtained. Then, the powder was heat at 550°C for 4 h with a heating rate of 2°C min^{-1} to obtain gCNS.

CoB was loaded by the impregnation-reduction method at 1, 3, 5, 7, 9, and 11 wt%. The amount of loaded CoB can be calculated by applying Equation A-1 to A-3 in Appendix A. Firstly, $CoCl_2.6H_2O$ was added to gCNS dissolved in DI water and the mixture was stirred for 1 h to allow Co^{2+} ions to attach on gCNS. After that, the mixture was reduced by adding $NaBH_4$ solution for 1 h to convert Co^{2+} on gCNS into amorphous CoB. Lastly, the mixture was washed and dried at 60°C for overnight to obtain the desirable sample.

3.2.2. 7NiB-gCNS in this research

In case of 7NiB-gCNS, every synthesis step and chemical substance are the same except Co^{2+} precursor is changed to $Ni(NO_3)_2.6H_2O$.

3.2.3. CoB-gCNS from Slovenia's laboratory

Melamine was used as the N_2-rich precursor to heat at 550°C for 4 h to obtain bulk gCN. Then, bulk gCN was grounded into powder. For the following step, bulk gCN was suspended in DI water with pulsed probe sonication for 15 min. Next, filtrating the mixture and dry it overnight to obtain gCNS. For CoB loading by impregnation-reduction method, 1, 3, 5, and 7%wt of CoB were applied. Firstly, $Co(NO_3)_2.6H_2O$ was added to gCNS dissolved in DI water and the mixture is stirred for 1 h to allow Co^{2+} ions to attach on gCNS. After that, the mixture was reduced by adding $NaBH_4$ solution for 1 h to convert Co^{2+} on gCNS into amorphous CoB. Lastly, the mixture was washed and dried overnight to obtain the final sample.

3.3. Photocatalytic Water Splitting Reaction

3.3.1. Instrument

3.3.1.1. Photocatalytic Reactor

300 ml Pyrex glass sealed on top with gas circulation system as a lid is used to contain photocatalyst sample and 10%vol TEOA solution for the water splitting reaction.

Figure 3-1 300 ml Pyrex glass reactor

3.3.1.2. Light Source

The visible light source is 300 W Xenon lamp with the AM 1.5G filter which shine light intensity from 550-600 mW/cm^2.

Figure 3-2 300W Xe lamp

3.3.1.3.   Gas Chromatography-Thermal Conductivity Detector (GC-TCD)
   Condition

In the research, the quantity of gas products from the water splitting reaction is analyzed by an online instrument consisting of GC (China Chromatography 2000) and TCD. The column inside the GC is MS-5A-3.5m column with the 20 ml/min flow rate of pure Argon gas as the carrier gas. The TCD electric current is adjusted to be 60 mA and injection, TCD, and oven temperature is 50^OC, 50^OC, and 60^OC, respectively.

Figure 3-3 Gas Chromatography (China Chromatography 2000) and Thermal Conductivity Detector

3.3.2. Experiment Process

CoB-gCNS sample in 10%vol 100 ml TEOA is redispersed in an ultrasonic cleanser for 20 min and is purged with Ar gas in the 300 ml vacuum sealed Pyrex glass reactor for 20 min to remove gases above the solution in the reactor. Then, the reactor wrapped with aluminum foil on the magnetic stirrer is shined by the visible light from 300 W Xe lamp to activate the photocatalytic hydrogen generation reaction. The reaction runs for 4 h and the HER rate results are collected for every 30 min.
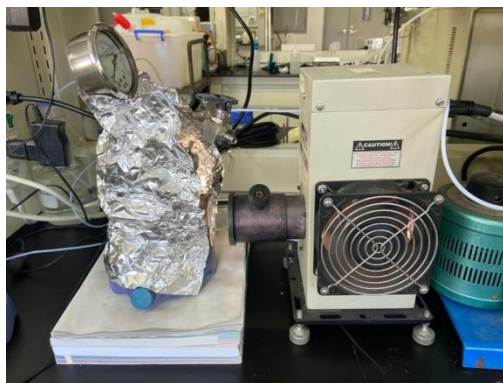
Figure 3-4 Photocatalytic hydrogen generation reaction setup

3.4. Characterization

3.4.1. X-Ray Diffraction (XRD)

Rigaku-Ultima IV is used to examine all photocatalyst samples for the microstructure and phase determination by operating with Cu-Kα1 radiation, 2θ = 5° - 80°, scan step is 0.01°, and the counting time 0.5 sec/step. The sample for the characterization is prepared by putting powder of photocatalyst on a glass plate.

3.4.2. Scanning Electron Microscopy (SEM) & Energy Dispersive X-Ray (EDX)

The morphology of the photocatalyst samples is obtained by SEM and EDX which is X-Max Oxford instrument. The condition of the instrument is 5 kV electron beam energy, and 8 mm working distance. The samples were prepared by attached to the plate by a carbon tape and coated with platinum for 15 min.

3.4.3. X-ray Photoelectron Spectroscopy (XPS)

XPS analysis is conducted by using Theta Probe of Thermo Scientific to reveal the surface chemical states of the photocatalyst samples. The sample powder is delivered to the staff of the instrument to conduct the characterization.

3.4.4. UV-vis Adsorption Spectroscopy (UV-Vis)

Light adsorption range and band gap energy of the photocatalyst samples are identified by the Aligent Cary 300 spectrometer. The condition of the measurement is setting the scanning rate at 240 nm/min between 250 nm to 800 nm. The sample is prepared by putting powder of the photocatalyst to the glass cylinder container.

3.4.5. Photoluminescence (PL) Intensity

The behavior of electron and hole (recombination rate) in the photocatalyst samples are investigated by observing the PL intensity (emission peak) resulted from the custom-build spectrophotometer. The wavelength that is applied to excite the electrons is 370 nm. The samples were prepared by mixing 3.5 mg of photocatalyst with 12 ml of DI water.

3.4.6. BET Surface Area

Specific Surface Area (SSA) is determined by the Brunauer–Emmett–Teller (BET) relying on N_2 adsorption on the photocatalyst samples. The applied instrument of this characterization is Micromeritics ASAP2010 and the operating condition is at 77.35 K. The sample is prepared by degas the powder of the photocatalyst at a room temperature.

3.4.7. Electrochemical Impedance Spectroscopy (EIS)

EIS is applied to identify the internal charge resistance of the photocatalyst which the resistance relates to the mobility of the charge. Metrohm Autolab is the instrument used to conduct this characterization. The samples were prepared by mixing 5 mg of photocatalyst with 150 µl of ethanol and 10 µl of nafion. 2 µl of sample is coated on the electrode. The applied frequency of the process is from 1 to 10^6 Hz with 2 V potential. Additionally, 300W Xe lamp with UV filtered is applied as the light source and 0.5 M Na_2SO_4 is electrolyte in the procedure.

Chapter 4
Result and Discussion

This chapter shows the result from the experiment, including characterizations (XRD, SEM, SSA, EDX, XPS, UV-Vis, PL, and EIS) and HER performance of all samples.

4.1. Morphology, Structure, and Chemical States of Samples

4.1.1. X-Ray Diffraction (XRD) Analysis

XRD patterns are shown in Figure 4-1. Two main peaks were observed at 2θ of 27.4° and extremely weak peak at 12.7°. The peak at 27.4° was associated with the stacking layers of 2D tri-s-triazine sheets, while the peak at 12.7° was associated with the in-plane repeating tri-s-triazine units of CNS [36]. No peak associated with CoB was observed as a result of high dispersion of CoB on gCNS surface [41]. Additionally, both peaks shrink as the amount of CoB increased. For peak at 27.4°, it is declined due to the attribution of the nucleation of CoB particles intercalating between the stacking layers of gCNS. In case of peak at 12.7°, the disappearance of this peak relates to the alternation of gCNS structure by loaded CoB particles [36].
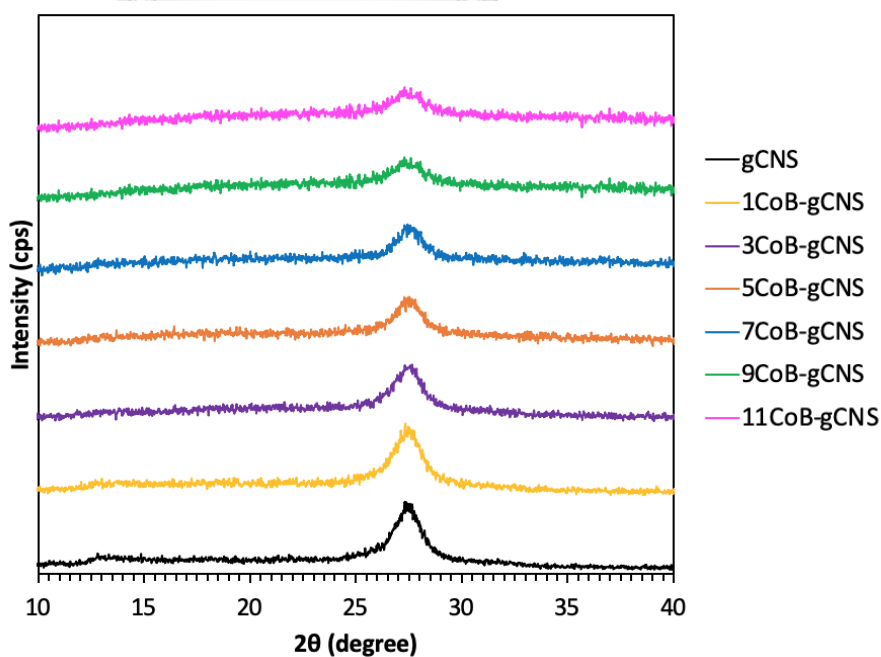

Figure 4-1 XRD Patterns of CoB-gCNS samples

4.1.2. Scanning Electron Microscopy (SEM)

From Figure 4-2, comparing SEM pictures at the same magnification of 50000x of (a) bulk gCN with (b) gCNS, it is readily apparent that big pieces of bulk gCN contain small flake-like plate of gCNS, while (b) gCNS structure possess a small flake structure. Focusing on Figure 4-2 (c) to (h), small particles which are CoB distributing on gCNS surface are observed. The higher CoB particles on gCNS in the figure (a) to (h) relates to the increase of CoB content (1 to 11 wt%).
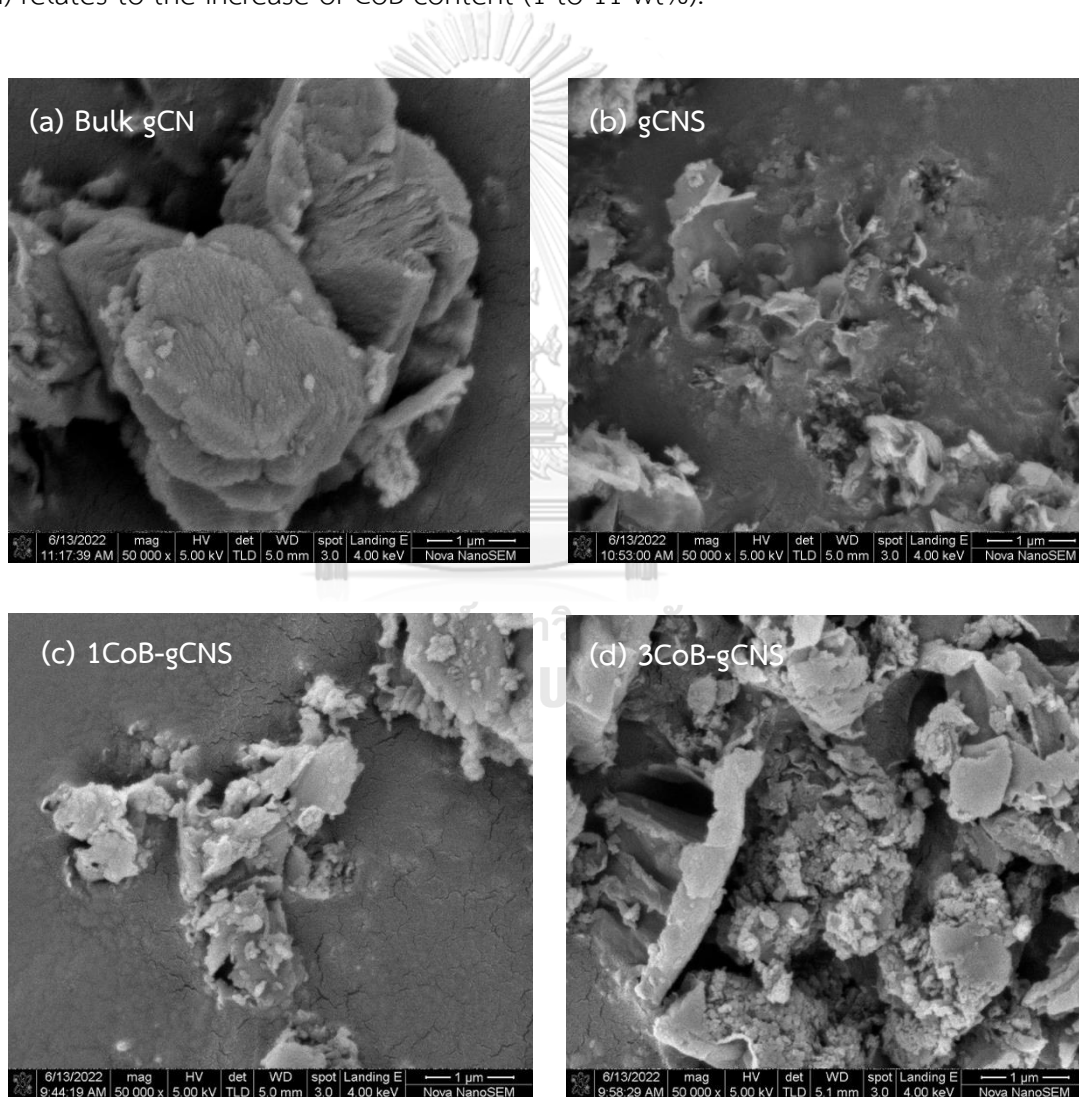

Figure 4-2 SEM images of (a) bulk gCN, (b) gCNS, (c) 1CoB-gCNS, (d) 3CoB-gCNS, (e) 5CoB-gCNS, (f) 7CoB-gCNS, (g) 9CoB-gCNS, and (h) 11CoB-gCNS
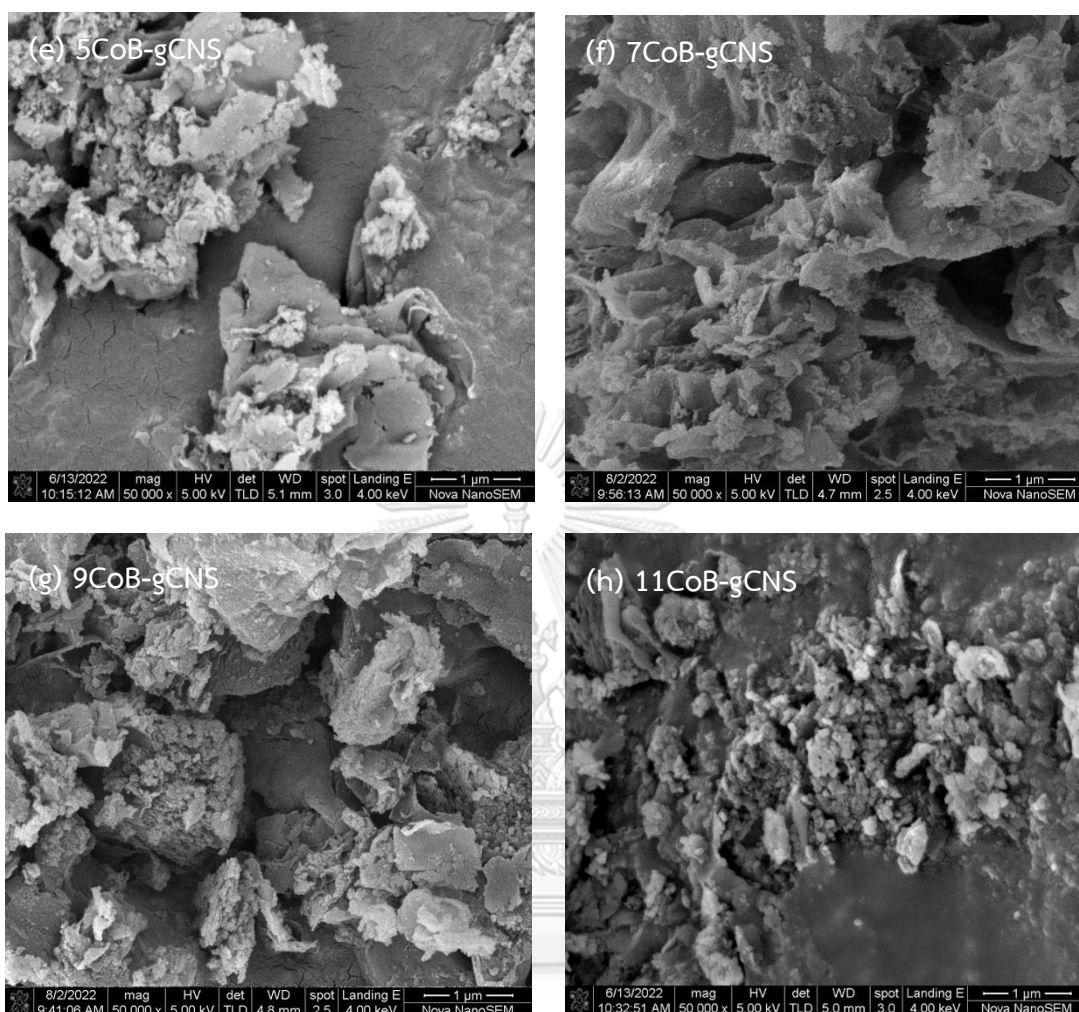
Figure 4-2 (continued) SEM images of (a) bulk gCN, (b) gCNS, (c) 1CoB-gCNS, (d) 3CoB-gCNS, (e) 5CoB-gCNS, (f) 7CoB-gCNS, (g) 9CoB-gCNS, and (h) 11CoB-gCNS

4.1.3. BET Surface Area and Element Content

Table 4.1-1 illustrates the SSA of all CoB-gCNS samples and 7NiB-gCNS. There is no particular pattern of SSA because gCNS in each CoB-gCNS samples are synthesized from different batch. However, the gCNS samples which were loaded by CoB show the decrease of SSA. In addition, gCNS, 7CoB-gCNS, 9CoB-gCNS, 11CoB-gCNS, and 7NiB-gCNS were systhesized with the same batch. Despite the different CNS batch, there is no significant effect to HER rate which is mention in the next section.

Table 4-1 BET surface area of CoB-gCNS samples and 7NiB-gCNS

Photocatalyst	gCNS	1CoB-gCNS	3CoB-gCNS	5CoB-gCNS	7CoB-gCNS	9CoB-gCNS	11CoB-gCNS	7NIB-gCNS
SSA (m^2/g)	90.8	82.1	76.9	50.8	77.3	71.5	69.3	61.5

Figure 4-3, EDX diagram is provided to confirm the successful loading of 1 to 11 wt% CoB on gCNS surface. The peak at around 2 keV is from coating platinum from the sample preparation before the characterization. The oxygen peak is from the oxidation of Co^{2+} from the ambient exposure.

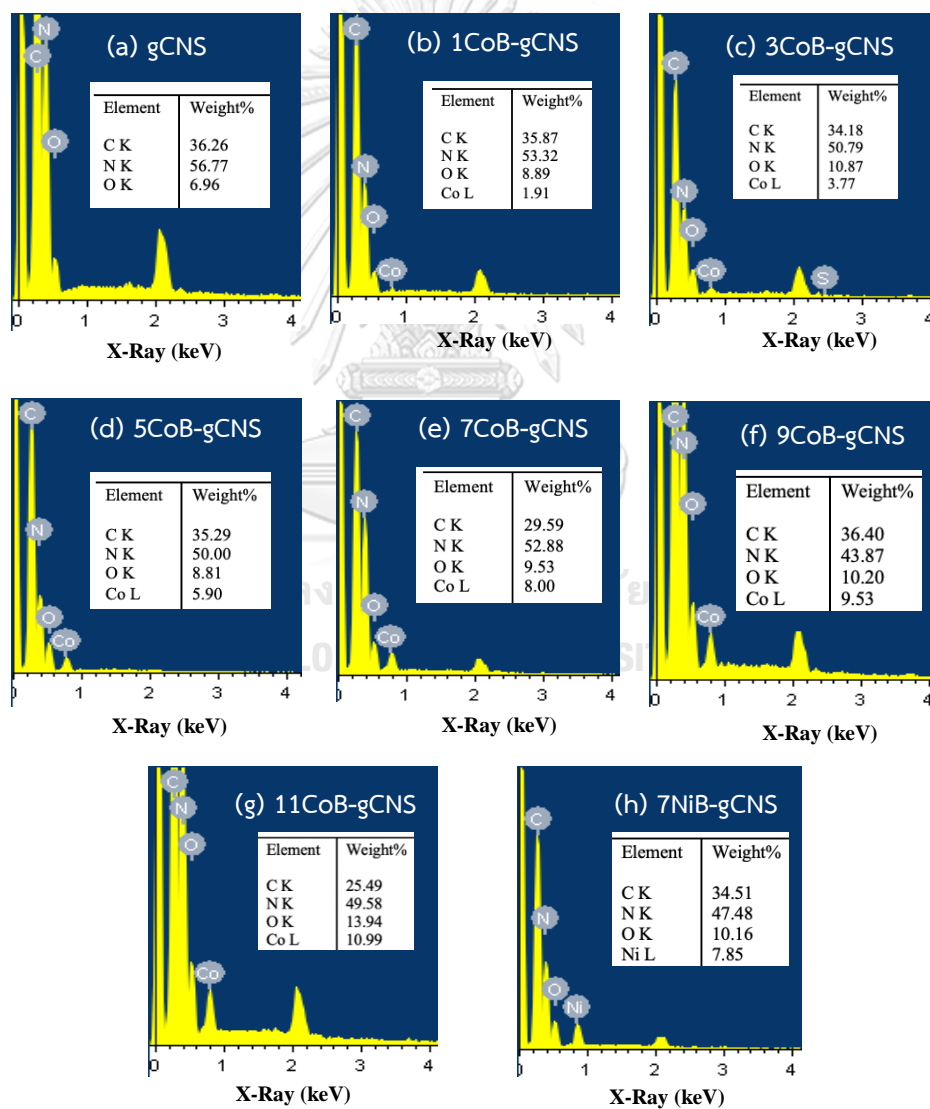**Figure 4-3** EDX spectra of (a) gCNS, (b) 1CoB-gCNS, (c) 3CoB-gCNS, (d) 5CoB-gCNS, (e) 7CoB-gCNS, (f) 9CoB-gCNS, (g) 11CoB-gCNS, and (h) 7NiB-gCNS

4.1.4. X-Ray Photoelectron Spectroscopy (XPS)

Figure 4-4 shows the XPS spectra of 9CoB-gCNS prior to the experiment, including peaks associated with C1s, N1s, Co2p, and B1s. C1s spectrum consisted of two distinct peaks at 284.5 eV and 287.9 eV which corresponded to C-C bonding and the bonding of N-C=N, respectively. For N1s spectrum, three peaks were observed, consisting of peaks of C-N=C (398.5 eV), $N-C_3$ (400 eV), and N-H (401.1 eV). Focusing on Co2p spectrum (see Figure 4-4c) since amorphous metal borides are spontaneously oxidized when exposed to air and water, the main peak at 780.7 eV corresponded Co-O bonding of Co $2p_{3/2}$ core level, while small peaks at 779.5 eV and 782.3 eV are from Co-B and Co-N bonding, respectively [42]. Additionally, broads peak at 786.0 eV and 803.4 eV are satellite peaks due to the removal of core
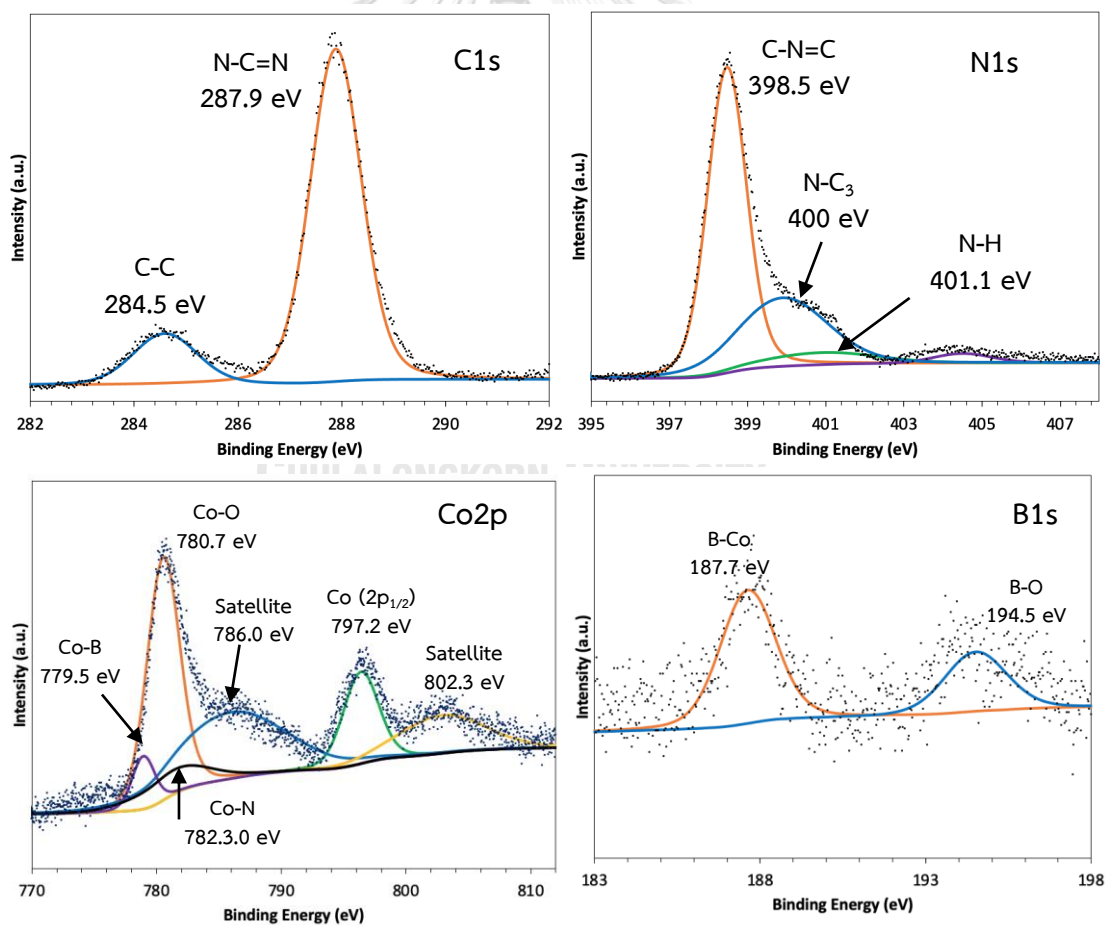
Figure 4-4 XPS patterns of fresh 9CoB-gCNS

electron by a photoionization passing through the valence band together with a sudden shift in coulombic charge during the measurement [43]. The peak at 797.2 eV corresponded to Co at $2p_{1/2}$ core levels. For the rest of B1s spectrum, two peaks are observed at 187.7 eV and 194.5 eV were associated with B-Co and B-O bonding, respectively.

Figure 4-5 shows the 4 XPS spectra of spent 9CoB-gCNS catalyst, including peaks associated with C1s, N1s, Co2p, and B1s. The peaks in the C1s and N1s remained the same. However, no peaks from Co2p and B1s were observed. The possible reason was that CoB particles were completely detached from the gCNS surface after the experiment, indicating poor stability [33].

Figure 4-5 XPS patterns of spent 9CoB-gCNS

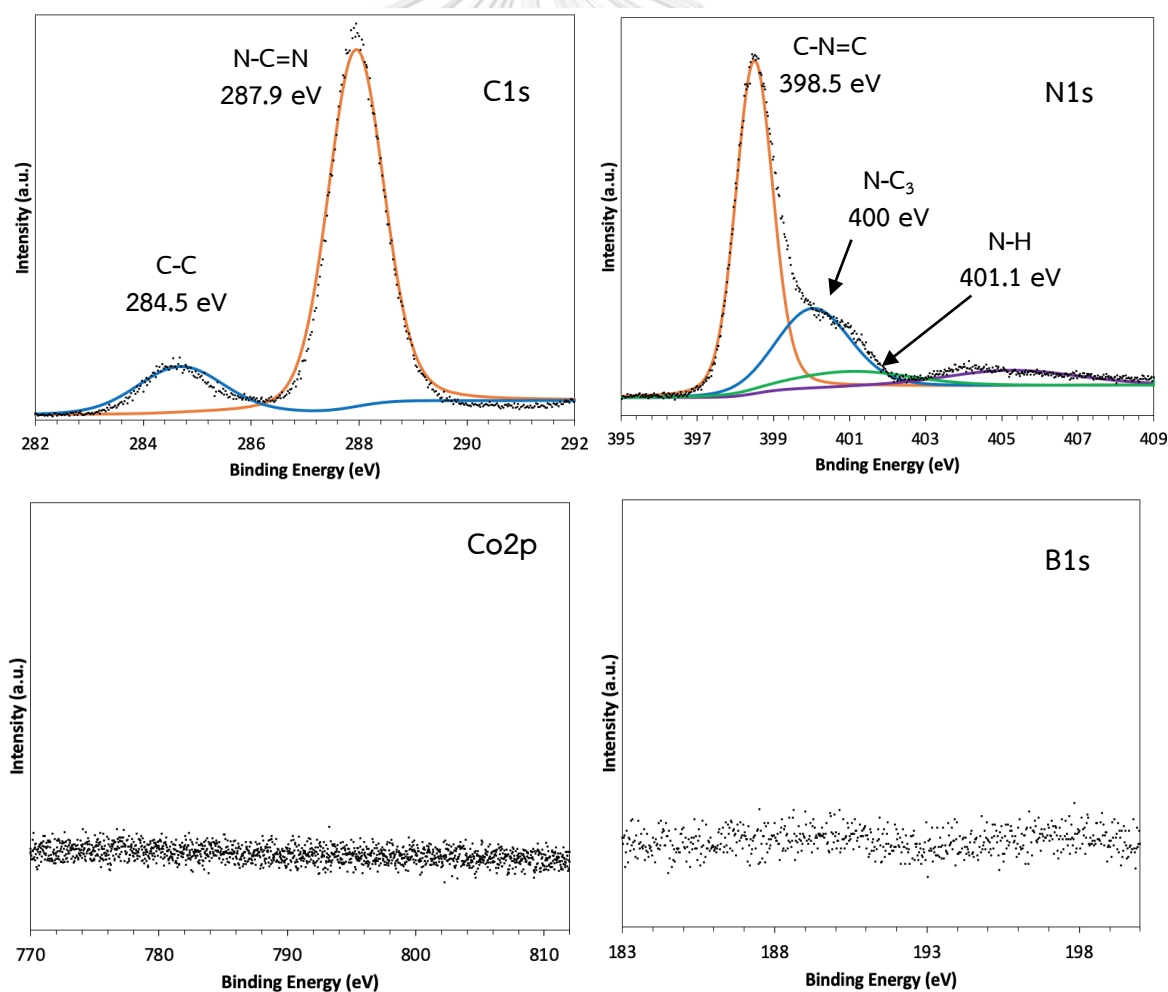XPS spectrums of fresh and spent 7NiB-gCNS photocatalyst were also investigated and demonstrated in Figure 4-6 and Figure 4-7, respectively. All peaks from C1s and N1s of both spent and fresh 7NiB-gCNS show similar peaks to those of 9CoB-gCNS from Figure 4-4 with a slightly shift of binding energy. For Ni2p spectrum in Figure 4-7, the main peak at 855.4 eV corresponded Ni-O bonding of Ni $2p_{3/2}$ core level, while small peaks at 854.7 eV and 856.9 eV are from Ni-B and Ni-N bonding, respectively. The peak at 873.9 eV corresponded to Co at $2p_{1/2}$ core levels. In addition, broads peak at 861.4 eV and 879.6 eV are satellite peaks. For B1s spectrum, two peaks are observed at 185.4 eV and 192.5 eV were associated with B-Ni and B-O bonding, respectively.

7NiB-gCNS provides much better stability than 9CoB-gCNS as shown in Ni2p and B1s spectrums in Figure 4-7. Bonding between Ni and N, Ni and B still exist after being used in the experiment which is the evidence that 7NiB-gCNS has better stability than 9CoB-gCNS [33]. This effect indicates that 7NiB-gCNS possesses higher photo-corrosion resistance than 9CoB-gCNS.
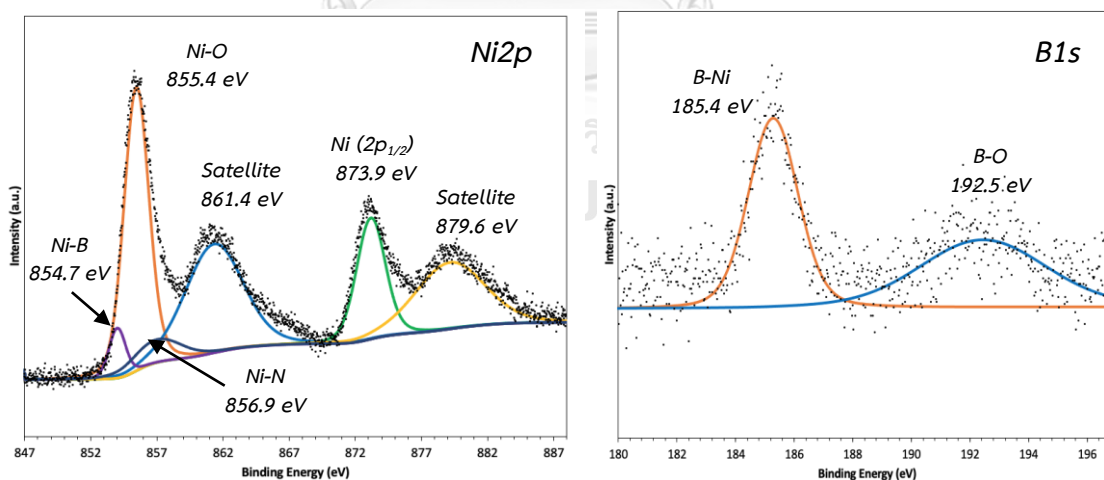
Figure 4-6 XPS patterns of fresh 7NiB-gCNS
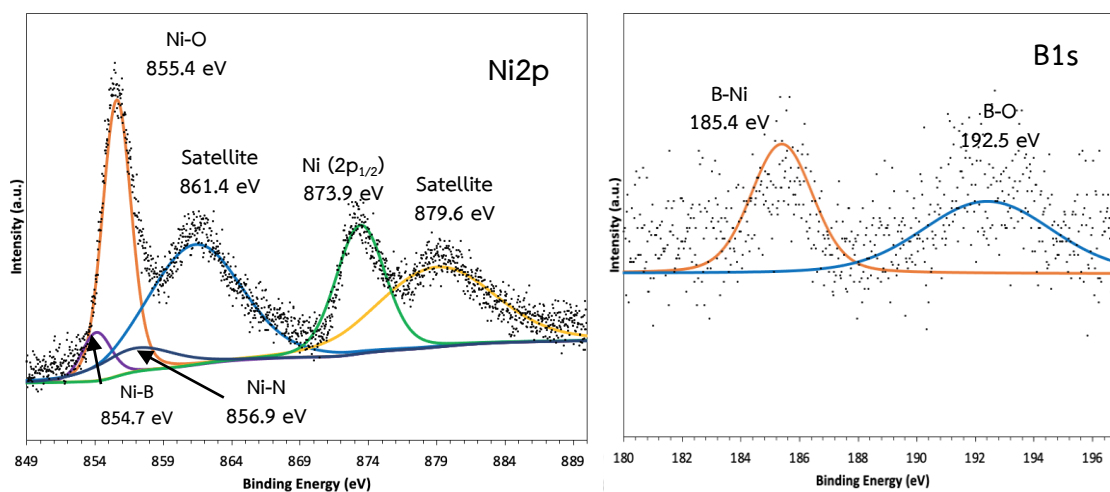
Figure 4-7 XPS patterns of spent 7NiB-gCNS

4.2. Optical Properties

4.2.1. Light Absorbance and Band Gap Energy

According to UV-visible spectrograms shown in Figure 4-8, the light absorption of CoB-gCNS between 400 to 700 nm was improved with increasing CoB loading. This was because of the deep dark brown color of CoB. The color of all CoB-gCNS samples and 7NiB-gCNS are shown in Figure 4-9. 9CoB-gCNS exhibited the greatest light absorbance in the visible region. Further CoB loading resulted in a drop in light absorption because excess amount of CoB particle will impede the light absorption as shown by 11CoB-gCNS [20].
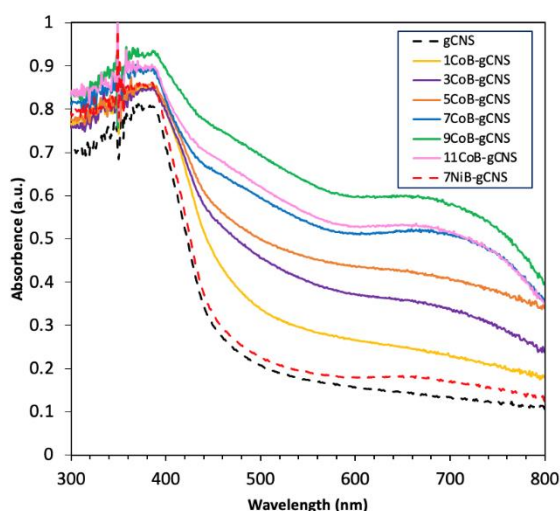
Figure 4-8 Light absorbance of various CoB-gCNS samples and 7NiB-gCNS

Figure 4-9 Colors of (a) gCNS, (b) 1CoB-gCNS, (c) 3CoB-gCNS, (d) 5CoB-gCNS, (e) 7CoB-gCNS, (f) 9CoB-gCNS, (g) 11CoB-gCNS, and (h) 7NiB-gCNS

The band gap energy of all samples that was determined from Kubelka-Munk plot is listed in Table 4-2. The calculation of the band gap is shown in Appendix C. The band gap of CoB-gCNS became narrower when the CoB loading was increased up to 9wt% and started to widen when the CoB loading was 11 wt%. The narrowing band gap from CoB loading was a result of CoB acts as the electron acceptor group lowering the conduction band resulting in smaller band gap. Consequently, the CoB-gCNS sample absorbed more light in visible region to generate H_2 [44].

Table 4-2 Band gap energy of CoB-gCNS samples and 7NiB-gCNS

Photocatalyst	Band Gap (eV)
gCNS	2.72
1CoB-gCNS	2.69
3CoB-gCNS	2.67
5CoB-gCNS	2.63
7CoB-gCNS	2.58
9CoB-gCNS	2.50
11CoB-gCNS	2.56
7NiB-gCNS	2.70

4.2.2. Photoluminescence Spectra

Figure 4-10 displays the photoluminescence spectra of various CoB-gCNS samples and 7NiB-gCNS. The excitation wavelength was applied to obtain the emission wavelength. The distinct emission peak detected at 450 nm corresponded to the electron-hole recombination rates. This peak started to quench when CoB content is loaded to gCNS. This was attributed to the enhancement of photogenerated electron trapping ability of CoB from conduction band of gCNS, resulting in slower recombination rate of electron and hole. The peak became the smallest when 9 wt% CoB was loaded on gCNS, suggesting the greatest potential to generate H_2. Thus, greater number of excited electrons could transport to active site on the surface of the photocatalyst and brought about in higher HER rate can be achieved with the loading of CoB.
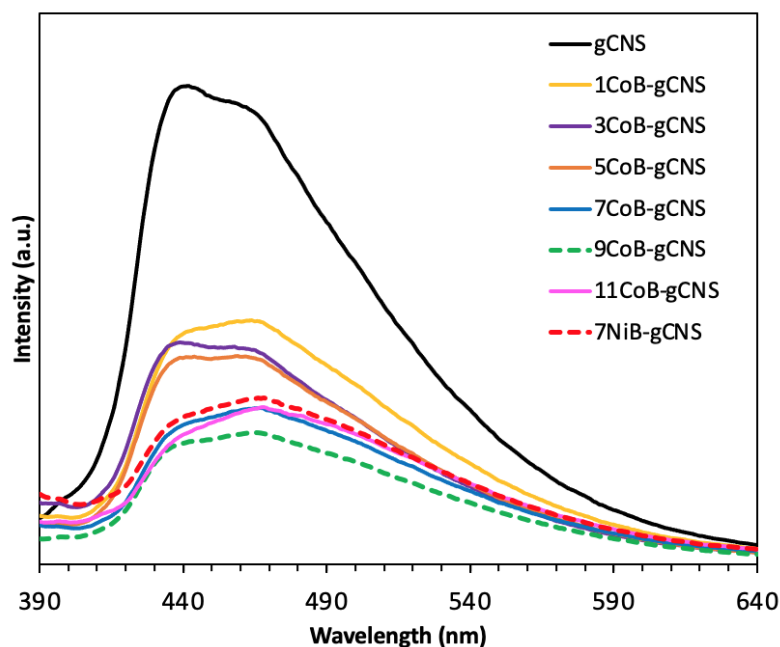

Figure 4-10 Photo Luminescence spectra of various CoB-gCNS samples and 7NiB-gCNS

4.2.3. Photoelectrochemical Impedance

The experiment set up of the electrode in electrolyte can be modelled as an equivalent electric circuit shown in Figure 4-11, where R_1 is charge transfer resistance, R_2 is electrolyte resistance, and C_1 is double layer capacitance. Hence, the total Z equation derived from Figure 4-11(a) is shown in Equation 4-1. Generally, the result of electrochemical impedance is shown as a semi-circle curve, where x axis denotes a real impedance and y axis denotes imaginary impedance (shown in Figure 4-11(b)). The value on X axis corresponds to R_1 and R_2 as a real Z (Z') and the value on Y axis corresponds to $i\omega C_1$ as an imaginary Z (Z") on a Nyquist plot. The radius of the semi-cycle is the total internal charge resistance of samples (R_1). If the radius is small, the charge resistance will be small, resulting in high mobility of charge transfer in the sample.
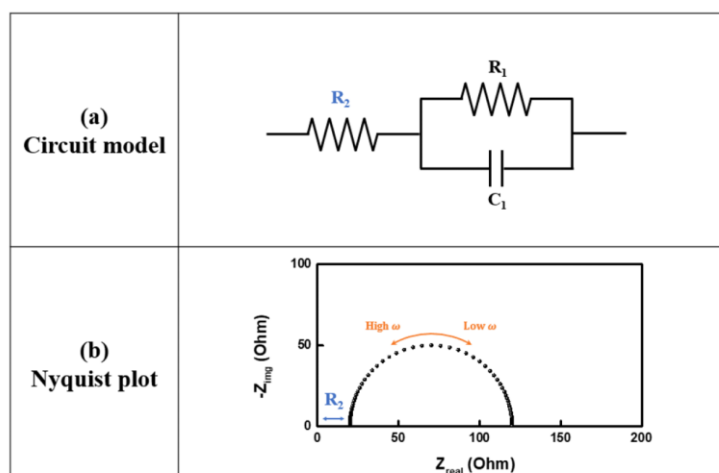
Figure 4-11 (a) Circuit model and (b) Nyquist plot of EIS [45]

$$Z = R_2 + \frac{R_1}{1+i\omega C_1 R_1} \qquad \text{Eq 4-1}$$

From Figure 4-12 a 9CoB-gCNS possessed the narrowest diameter among other semicircles indicating the smallest internal charge transfer resistance, while gCNS provided the largest resistance. Consequently, electron mobility in 9CoB-gCNS

is the fastest which means more electrons can travel to the active site at CoB and fasten HER rate. Further CoB doping beyond 9CoB (11wt% CoB) varied the curve upward. Additionally, from Figure 4-12 b, 7NiB-gCNS semicircle possesses wider diameter than that of 9CoB-gCNS.

Figure 4-12 (a) EIS Nyquist plots of CoB-gCNS samples and (b) 7NiB-gCNS versus 9CoB-gCNS

4.3. Hydrogen Generation Performance

4.3.1. HER rate of Slovenia's samples

The result shown in Figure 4-13 are HER performance from 0, 1, 3, 5, and 7 wt% CoB, and 7 wt% NiB loaded on gCNS synthesized in the Slovenia's lab. From Figure 4-13 (a), 7CoB-gCNS possessed the best HER rate (31.54 µmole/g/h) which was 30 folds higher than that of gCNS 30 folds. Despite the provided result, it cannot be concluded that 7CoB-gCNS posse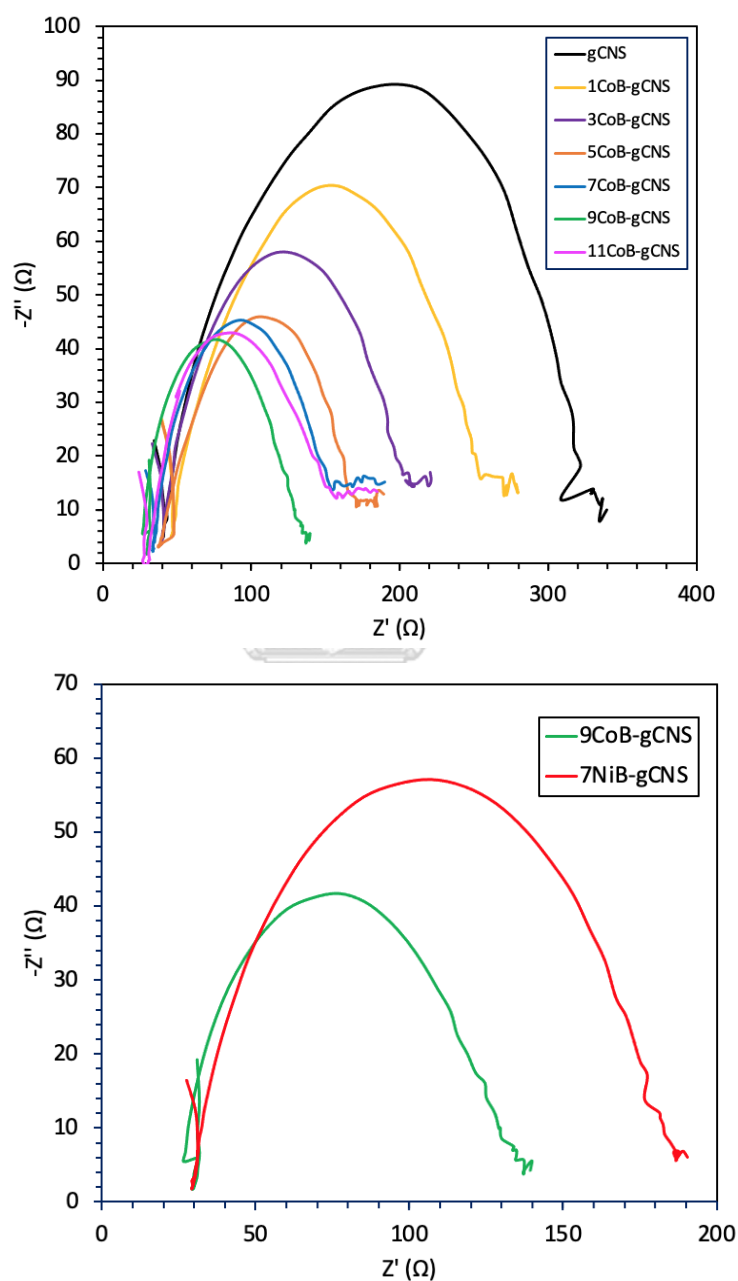ssed the highest HER rate until the sample with higher CoB loading was done. In addition, all CoB-gCNS samples required 60 to 90 min to begin generating hydrogen as shown in Figure 4-13 (b). This may be a result of the samples surface being oxidized to form core (CoB particle) and oxide shell $(Co(OH)_2)$ structure [42]. Consequently, certain times was needed in order to reduce the surface of CoB-gCNS sample to be active. Although the result was positive, the HER rate of 7CoB-gCNS H_2 was considerably slower than 7NiB-gCNS. Furthermore, 7NiB-gCNS immediately generated H_2 after being exposed to light. This is because 7NiB-gCNS exhibited higher electron mobility, facilitating electrons to transport from CNS to NiB active sites faster. As a result, the trapping mechanism of electrons in the conduction band was enhanced (i.e., lower recombination rate from the conduction band) and the HER rate is faster.
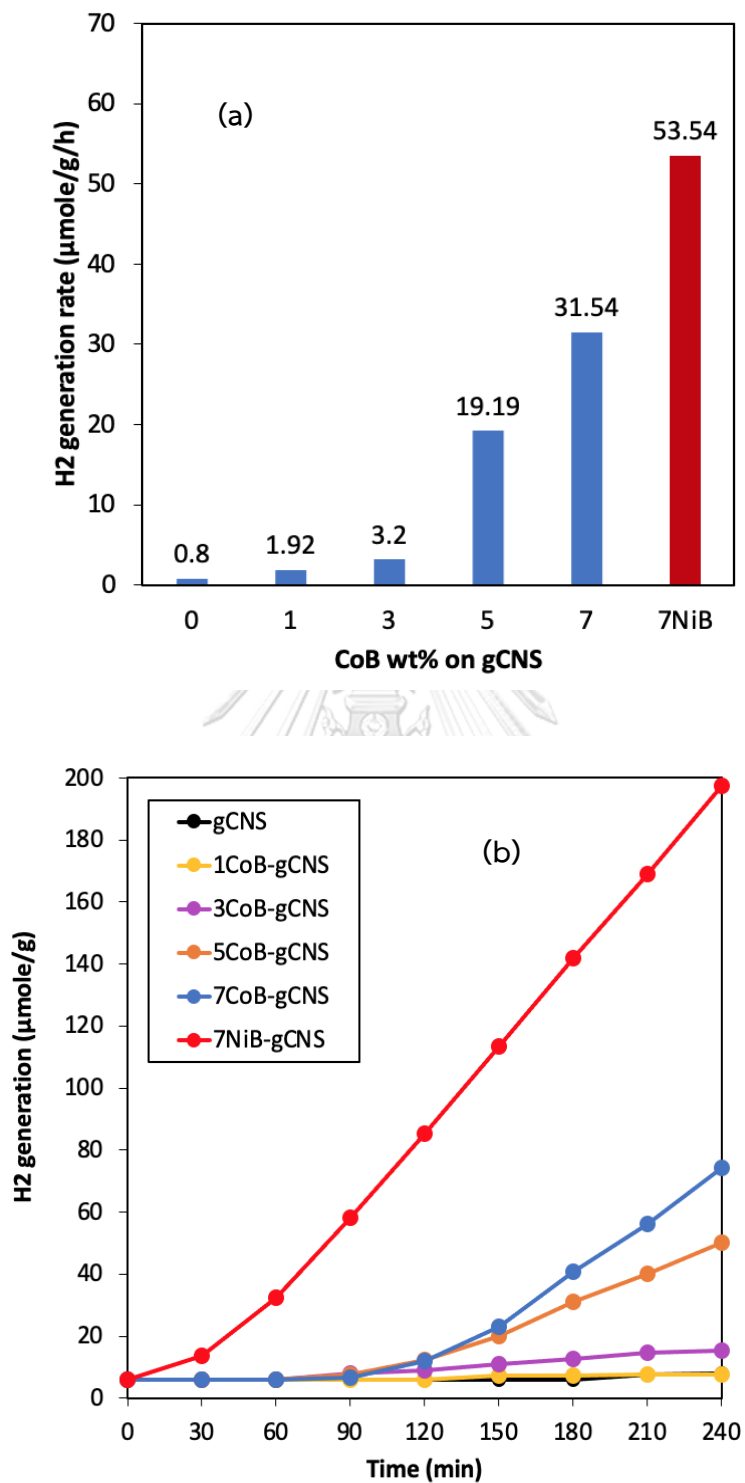
Figure 4-13 (a) H_2 generation rate and (b) H_2 generation trend of Slovenia's samples

4.3.2. HER rate from CoB-gCNS and NiB-gCNS synthesized for this research

The result shown in Figure 4-13 are HER performance from 1, 3, 5, 7, 9, 11 wt% CoB, and 7 wt% NiB loaded on gCNS. According to Figure 4-14 (a), an increase in CoB loading up to 9wt% on CNS enhanced HER rate up to 60.71 μmole/g/h as the highest HER rate among CoB-gCNS catalysts. However, when CoB loading exceeded 9 wt%, the HER rate dropped slightly. This is attributed to 9CoB-gCNS possessing the lowest recombination rate of excited electron (as shown in Figure 4-10) and the best light absorption in the visible region (As shown in Figure 4-8). Nevertheless, from Figure 4-14 (b), 9CoB-gCNS still required about 30 min to begin generating H_2 whereas 7NiB-gCNS immediately generated H_2 after being irradiated. However, light absorption and band gap energy of the photocatalyst were not key factors for obtaining high HER rate. Although 7NiB-gCNS obviously exhibited lower visible light absorption than CoB-gCNS did, its HER rate was far superior to those of CoB-gCNS samples with CoB loading lower than 7wt%. Consequently, the recombination rate and electron mobility were key factors for the fast HER rate.
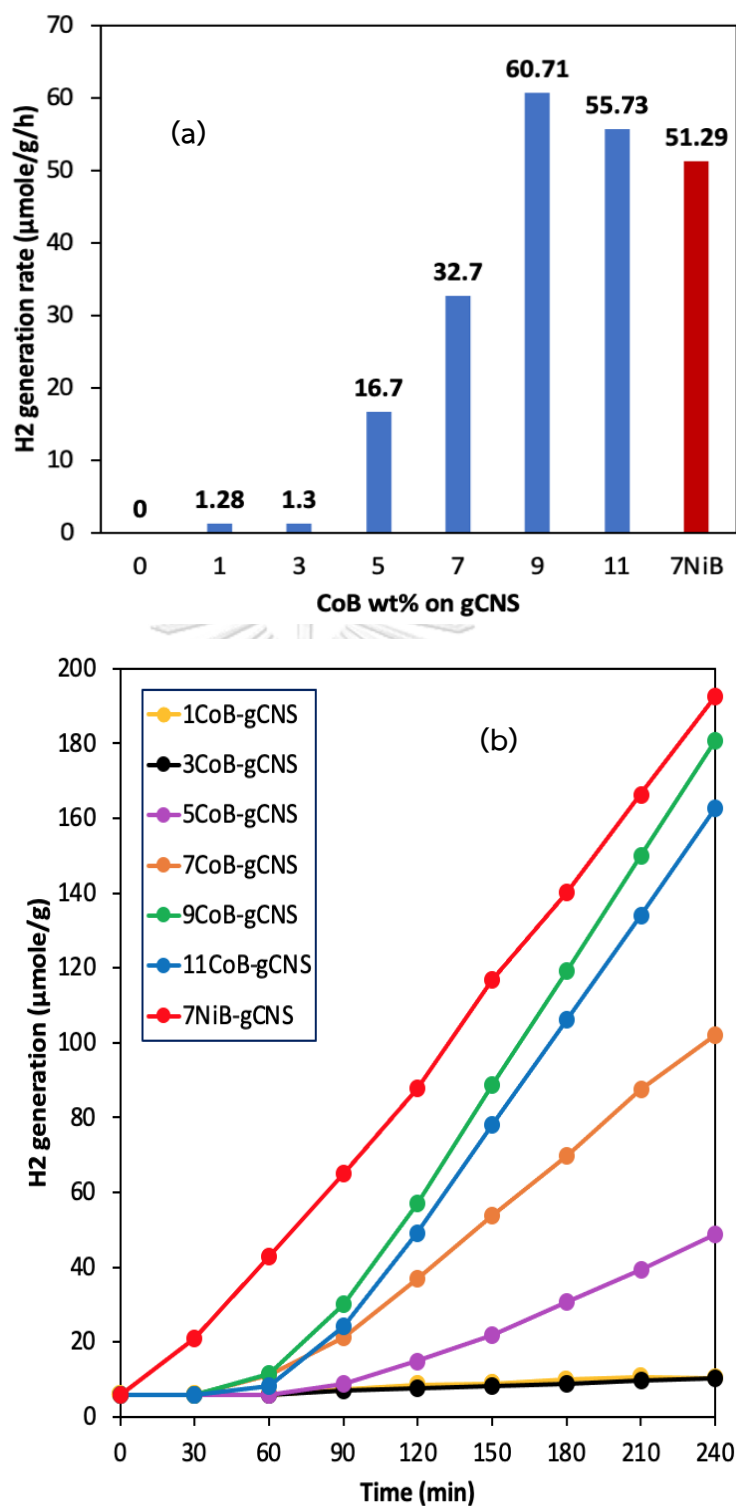
Figure 4-14 (a) H_2 generation rate and (b) H_2 generation trend of CoB-gCNS samples and 7NiB-gCNS

Additionally, HER performance of 7NiB-gCNS and 9NiB-gCNS as shown in Figure 4-15. This experiment was conducted to investigate the effect from increasing NiB content from 7 to 9 wt% because increasing CoB content from 7 to 9 wt% can enhance better HER performance of gCNS. Regarding Figure 4-15, 7NiB-gCNS shew better HER performance than 9NiB-gCNS. This result was also claimed in the previous research about NiB-gCNS as well [20].
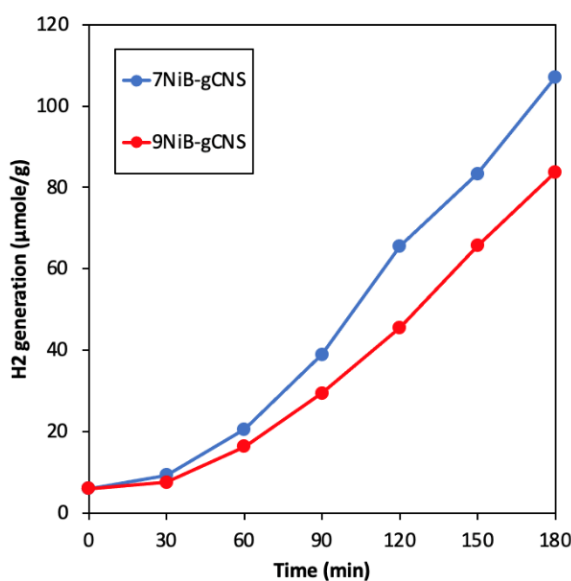
Figure 4-15 Hydrogen generation trend of 7NiB-gCNS and 9NiB-gCNS

4.3.2.1.   Stability Test

9CoB-gCNS was applied in three methods for the stability test. For the first method, the stability test was continuously conducted in the same reactor without opening its lid to change the solution (DI water and TEOA) in the reactor for 20 h of irradiation. The reactor was purged every 4 h to remove the residual gas to start the new cycle of stability test. For the second method, after finishing the first 4 h irradiation, the reactor was opened to wash the spent 9CoB-gCNS with DI water. Spent solution was replaced by fresh DI water and TEOA for the next 4 h irradiation of the second cycle of stability test. For the third method, after the first 4 h irradiation to 9CoB-gCNS had been finished, the spent solution (DI water and TEOA) was filter from the reactor. Then, only spent solution without adding 9CoB-gCNS was irradiated for the second cycle of stability test.

Form Figure 4-16 (a), the stability of the first method began to decline after the third recycle as a result of CoB particle detaching from gCNS surface. However, from Figure 4-16 (b), the stability of 9CoB-gCNS of the second method was significantly plunged. This may inform that CoB particle one 9CoB-gCNS detached into the solution during the H_2 generation reaction and the bonding between CoB and gCNS is reversible which makes 9CoB-gCNS still can generate H_2. On the other hand, after filtrated 9CoB-gCNS from the solution after the first trial, all CoB particles may be gone with the solution. The second method result relates to the XPS pattern from Figure 4-5 that no Co^{2+} and B peak were detected from the Co2p and B1s spectra.

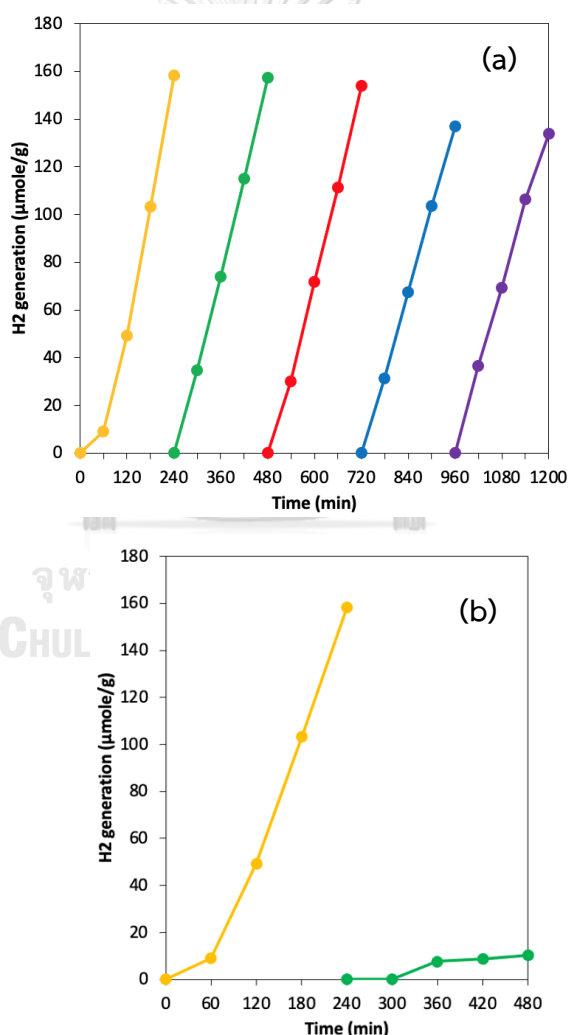**Figure 4-16** Stability test of 9CoB-gCNS (a) the first method and (b) the second method

From Figure 4-17, the spent solution with leaching CoB content did not show any H_2 generation. It indicates that CoB alone could not produce any H_2. Consequently, CoB has to be loaded to gCNS or other photocatalyst to enhance HER performance as a cocatalyst.
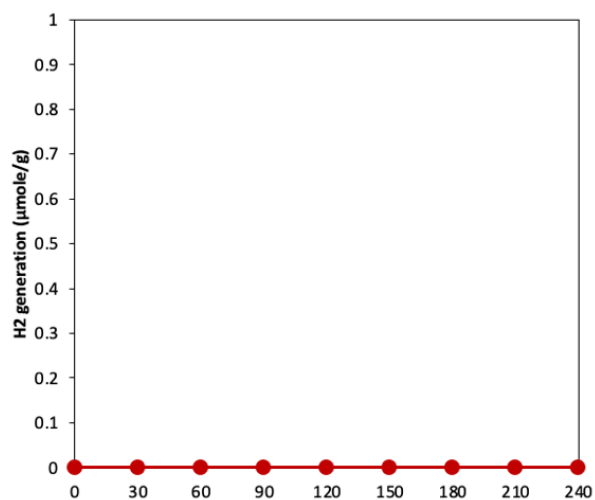

Figure 4-17 H_2 generation amount from the third stability method

Chapter 5
Conclusion and Recommendation

In this research, graphitic carbon nitride nanosheet (gCNS) was synthesized by one-step exfoliation method and 1 to 11 wt% of cobalt boride (CoB) was loaded on gCNS by impregnation reduction method to enhance H_2 evolution reaction (HER) rate. According to the result, 9wt% CoB loaded on CNS (9CoB-gCNS) produced the highest HER rate (60 µmole/g/h), which was about 75 times faster than the HER rate of gCNS (0.8 µmole/g/h) 60 times. This is because the optimum CoB content loaded on CNS influence higher light absorbance in the visible range and reduces band gap energy. Moreover, the recombination rate of excited electron from the conduction band is the narrowest because 9wt% CoB can provide the highest efficiency of electron trapping ability of CoB on gCNS in the conduction band as well as the highest mobility of electron proved from the lowest internal charge resistance from the Nyquist plot. These effects attract more electron to the active site of CoB-gCNS samples leading to higher HER rate. Nevertheless, the increment loading of CoB (more than 9wt%) causes the decreasing HER rate regarding to high agglomeration of CoB particle which block the surface-active sites and impede the light absorption area of CoB-gCNS. Moreover, the higher recombination rate and lower electron mobility are observed from the excess CoB loading. In addition, the CoB bonding with gCNS is possibly reversible which CoB particle is dissolved into the solution, while HER rate still increases. Comparing 9CoB-CNS to 7NiB-CNS, 9CoB-CNS shows slightly higher HER performance due to better mentioned properties. However, great light absorbance and narrow band gap effects are not as vital as low recombination rate and electron mobility.

For the further research and recommendation, CoB-gCNS and NiB-gCNS can be calcined to observe the possibility of greater HER performance. Furthermore, loading mix transition metal between Ni and Co boride with optimum weight ratio to gCNS may also enhance HER performance of the photocatalyst.

Appendices

Appendix A   Calculation for different CoB content loading on gCNS

First of all, amount of gCNS for each one synthesis of CoB-gCNS sample is 300 mg. According to Table A-1, Co^{2+} content in Co^{2+} precursor ($CoCl_2.6H_2O$) is 24.78%. Hence. Weight in g of Co^{2+} in metal precursor (X) is 24.78% times weight of applied Co^{2+} precursor (Y) shown in Eq A-1.

Table A-1 Chemical Substances and molecular weight

Chemical Substance	Weight (g/mole)
$CoCl_2.6H_2O$	237.83
$NaBH_4$	37.8
Co^{2+}	58.93
B	10.81

$$X = (\frac{24.78}{100}) \cdot Y \qquad \text{(Eq A-1)}$$

For B content in CoB, the ratio of Co^{2+} and B is 1 to 1. To calculate amount of B for CoB synthesis (Z), weight in g of Co^{2+} in metal precursor (X) is multiplied by molecular weight of B over molecular weight of Co^{2+} for 1 to 1 ratio shown in Eq A-2.

$$Z = X \cdot \frac{58.93}{10.81} \qquad \text{(Eq A-2)}$$

However, excess amount of B precursor is applied to confirm a whole reduction of Co^{2+} on CNS. Consequently, wt% of CoB in CoB-CNS (K) for each synthesis is shown in Eq A-3. Additionally, these three equations are functionalized in Excel conveniently obtain applied Co^{2+} precursor (Y).

$$K = \frac{X+Z}{300+X+Z} \cdot 100\% \qquad \text{(Eq A-3)}$$

Appendix B   Calculation of H_2 Quantity from the Experiment

The calibration curve is required for converting area (UV*sec) of H_2 peak analyzed by GC-TCD to concentration (mole). The calibration curve is constructed by applying ideal gas law (Eq B-1) to calculate the selected H_2 volume in syringe injecting in the GC. H_2 gas tank (0.3% of H_2 and 99.7% of Ar) used as the H_2 source for the calibration curve (as shown in Figure B-1).

(Eq B-1)
$$n = \frac{Pv}{rt} = \frac{1\ atm * v\ of\ syringe\ ml * \frac{1\ l}{1000\ ml}}{0.082\ \frac{l*atm}{K*mole} * 299\ K} * 0.3\% = x\ mole$$

In this research, five volumes (0.05, 0.1, 0.15, 0.2, and 0.25 ml) of a syringe are used for the calculation. For each volume, H_2 gas is withdrawn from the H_2 gas tank and inject to the GC to calculate peak area of H_2 gas and repeating this step for three times to find the average peak area of H_2.

Table B-1 Data of the calibration curve

Volume of the syringe (ml)	Amount of H_2 (Mole)	Area (UV*Sec)		
0.25	0.03059	342463	347331	344361
0.20	0.024472	275338	274786	274681
0.15	0.018354	203819	203490	202175
0.10	0.012236	133941	133446	133932
0.05	0.006118	66415	66223	66110
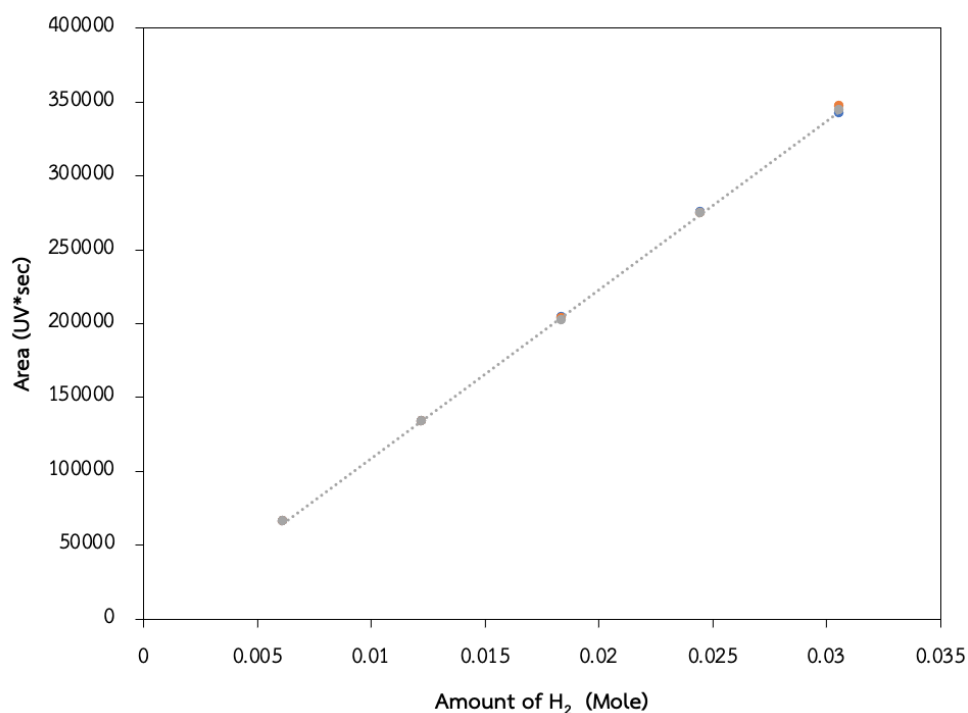
Figure B-1 Calibration Curve

The linear equation of calibration curve from Figure B-1 is shown in Eq B-2 which Y is Area (UV*Sec) and X is amount of H_2 (µmole).

$$Y = (1.14 \times 10^7)X - 4923.5 \qquad \text{(Eq B-2)}$$

Hence, to convert the equation to find amount of H_2 from peak area from GC is shown in Eq B-3.

$$X = \frac{Y + 4923.5}{1.14 \times 10^7} \qquad \text{(Eq B-3)}$$

In addition, Eq B-3 has to be multiplied by 210 over 0.3 because the void above solution in the reactor is 210 ml and sample loop in GC is 0.3 ml and multiplied by 0.05 to change the unit to µmole/g because 0.05 g of photocatalyst is applied in each experiment. Hence, the final equation to obtain the quantity of generated H_2 from the experiment is shown in Eq B-4.

$$X = \frac{Y+4923.5}{1.14\times10^7}\,(\mu mole) \cdot \frac{210\ ml}{0.3\ ml} \cdot \frac{1}{0.05\ g} \qquad \text{(Eq B-4)}$$

To calculate the HER rate from Eq B-4, X from each period from 0 to 240 min has to be plotted to obtain a linear graph. Then, the slope of that particular curve is HER rate of that sample which is multiplied by 60 to obtain HER rate in μmole/g/h unit.

Appendix C   Band Gap Energy Calculation

To obtain the band gap energy of the photocatalyst in this research, Remission function (F(R)) versus wavelength data is required to generate Kubelka-Munk plot. The X axis of Kubelka-Munk plot corresponds to photon energy (hv) which can be calculated by Equation C-1, where λ is wavelength (nm). The Y axis of Kubelka-Munk plot corresponds to the value which can be calculated by Equation C-2. Consequently, the bandgap energy is the interception of the linear slope of the steepest part of the curve of the Kulbelka-Munk plot to the X axis. In addition, Kulbelka-Munk plot of every CoB-gCNS and 7NiB-gCNS are shown in Figure C-1.

$$hv = \frac{1239.8}{\lambda} \qquad \text{(Eq. C-1)}$$

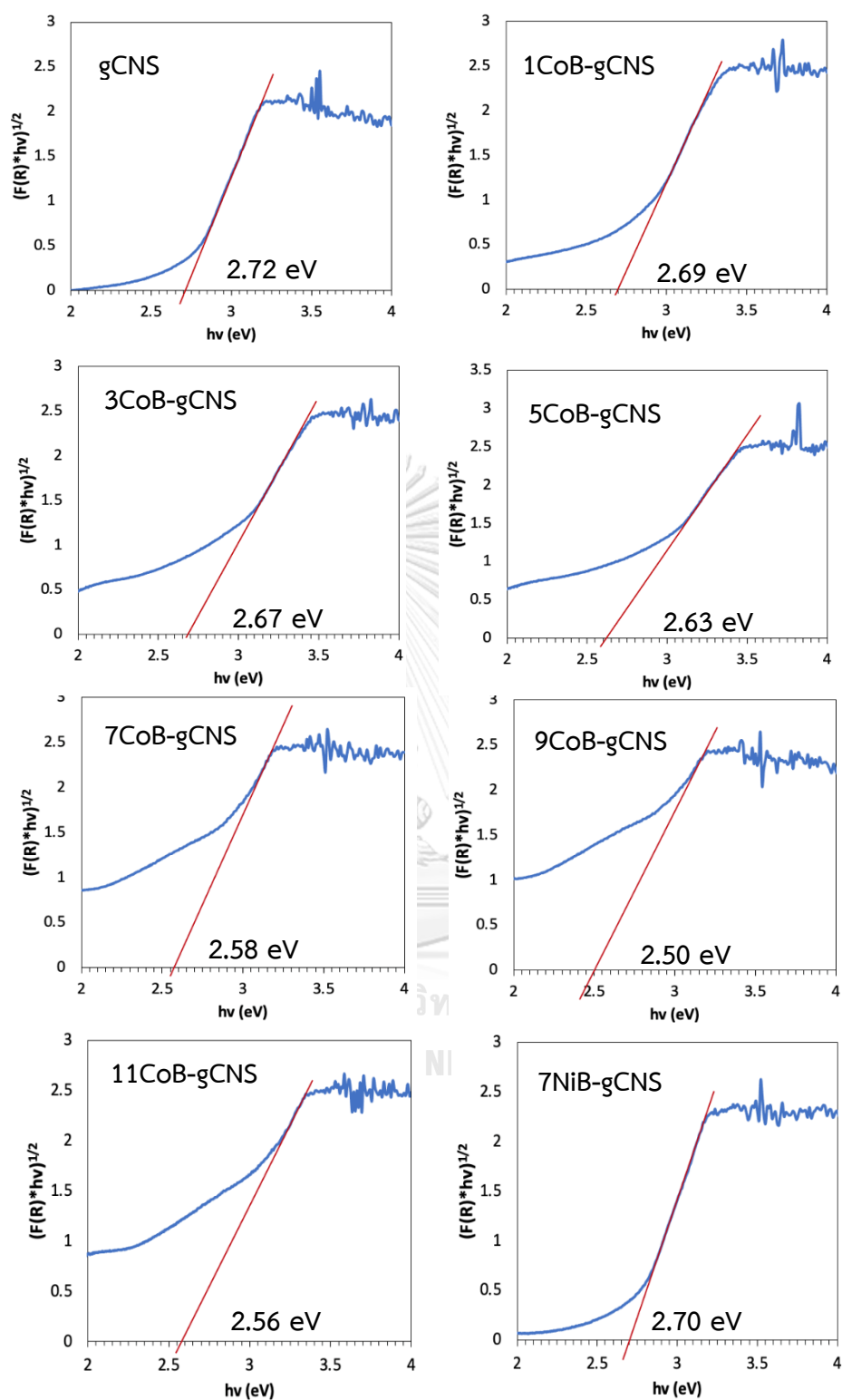$$Y\ axis = (F(R) * hv)^{1/2} \qquad \text{(Eq. C-2)}$$

Figure C-1 Kubelka-Munk plot of CoB-gCNS samples and 7NiB-gCNS

REFERENCES

1. Endo, N., K. Goshome, M. Tetsuhiko, Y. Segawa, E. Shimoda, and T. Nozu, *Thermal management and power saving operations for improved energy efficiency within a renewable hydrogen energy system utilizing metal hydride hydrogen storage.* International Journal of Hydrogen Energy, 2021. **46**(1): p. 262-271.

2. Singh, R., A. Altaee, and S. Gautam, *Nanomaterials in the advancement of hydrogen energy storage.* Heliyon, 2020. **6**(7): p. e04487.

3. Farrell, A.E., D.W. Keith, and J.J. Corbett, *A strategy for introducing hydrogen into transportation.* Energy Policy, 2003. **31**(13): p. 1357-1367.

4. Liao, C.-H., C.-W. Huang, and J. Wu, *Hydrogen production from semiconductor-based photocatalysis via water splitting.* Catalysts, 2012. **2**(4): p. 490-516.

5. Kudo, A. and Y. Miseki, *Heterogeneous photocatalyst materials for water splitting.* Chemical Society Reviews, 2009. **38**(1): p. 253-278.

6. Fujishima, A. and K. Honda, *Electrochemical photolysis of water at a semiconductor electrode.* nature, 1972. **238**(5358): p. 37-38.

7. Yu, J., Q. Li, S. Liu, and M. Jaroniec, *Ionic‐liquid‐assisted synthesis of uniform fluorinated B/C‐codoped TiO2 nanocrystals and their enhanced visible‐light photocatalytic activity.* Chemistry–A European Journal, 2013. **19**(7): p. 2433-2441.

8. Jang, E.S., J.H. Won, S.J. Hwang, and J.H. Choy, *Fine tuning of the face orientation of ZnO crystals to optimize their photocatalytic activity.* Advanced Materials, 2006. **18**(24): p. 3309-3312.

9. Liu, S., G. Huang, J. Yu, T.W. Ng, H.Y. Yip, and P.K. Wong, *Porous fluorinated SnO2 hollow nanospheres: transformative self-assembly and photocatalytic inactivation of bacteria.* ACS applied materials & interfaces, 2014. **6**(4): p. 2407-2414.

10. Zhou, X., Q. Xu, W. Lei, T. Zhang, X. Qi, G. Liu, K. Deng, and J. Yu, *Origin of Tunable Photocatalytic Selectivity of Well‐Defined α‐Fe2O3 Nanocrystals.* Small, 2014. **10**(4): p. 674-679.

11.   Xiang, Q., B. Cheng, and J. Yu, *Hierarchical porous CdS nanosheet-assembled flowers with enhanced visible-light photocatalytic H2-production performance.* Applied Catalysis B: Environmental, 2013. **138**: p. 299-303.

12.   Liu, S., K. Yin, W. Ren, B. Cheng, and J. Yu, *Tandem photocatalytic oxidation of Rhodamine B over surface fluorinated bismuth vanadate crystals.* Journal of Materials Chemistry, 2012. **22**(34): p. 17759-17767.

13.   Huang, W.-C., L.-M. Lyu, Y.-C. Yang, and M.H. Huang, *Synthesis of Cu2O nanocrystals from cubic to rhombic dodecahedral structures and their comparative photocatalytic activity.* Journal of the American Chemical Society, 2012. **134**(2): p. 1261-1267.

14.   Wang, Y., Q. Wang, X. Zhan, F. Wang, M. Safdar, and J. He, *Visible light driven type II heterostructures and their enhanced photocatalysis properties: a review.* Nanoscale, 2013. **5**(18): p. 8326-8339.

15.   Takanabe, K., *Photocatalytic water splitting: quantitative approaches toward photocatalyst by design.* ACS Catalysis, 2017. **7**(11): p. 8006-8022.

16.   Masih, D., Y. Ma, and S. Rohani, *Graphitic C3N4 based noble-metal-free photocatalyst systems: a review.* Applied Catalysis B: Environmental, 2017. **206**: p. 556-588.

17.   Ye, S., R. Wang, M.-Z. Wu, and Y.-P. Yuan, *A review on g-C3N4 for photocatalytic water splitting and CO2 reduction.* Applied Surface Science, 2015. **358**: p. 15-27.

18.   Cao, S., J. Low, J. Yu, and M. Jaroniec, *Polymeric photocatalysts based on graphitic carbon nitride.* Advanced Materials, 2015. **27**(13): p. 2150-2176.

19.   He, F., G. Chen, Y. Zhou, Y. Yu, L. Li, S. Hao, and B. Liu, *ZIF-8 derived carbon (C-ZIF) as a bifunctional electron acceptor and HER cocatalyst for gC 3 N 4: construction of a metal-free, all carbon-based photocatalytic system for efficient hydrogen evolution.* Journal of Materials Chemistry A, 2016. **4**(10): p. 3822-3827.

20.   Zhu, Q., B. Qiu, M. Du, M. Xing, and J. Zhang, *Nickel Boride Cocatalyst Boosting Efficient Photocatalytic Hydrogen Evolution Reaction.* Industrial & Engineering Chemistry Research, 2018. **57**(24): p. 8125-8130.

21.   Farquhar, G.D., S. Von Caemmerer, and J.A. Berry, *Models of photosynthesis.*

Plant physiology, 2001. **125**(1): p. 42-45.

22. Maeda, K., *Photocatalytic water splitting using semiconductor particles: History and recent developments.* Journal of Photochemistry and Photobiology C: Photochemistry Reviews, 2011. **12**(4): p. 237-268.

23. Hisatomi, T., K. Takanabe, and K. Domen, *Photocatalytic Water-Splitting Reaction from Catalytic and Kinetic Perspectives.* Catalysis Letters, 2015. **145**(1): p. 95-108.

24. Zheng, Y., J. Liu, J. Liang, M. Jaroniec, and S.Z. Qiao, *Graphitic carbon nitride materials: controllable synthesis and applications in fuel cells and photocatalysis.* Energy & Environmental Science, 2012. **5**(5): p. 6717-6731.

25. Yue, L., W. Yihan, P. Hongwei, W. Xiangxue, Y. Shujun, and W. Xiangke, *Study on the removal of water pollutants by graphite phase carbon nitride materials.* Progress in Chemistry, 2019. **31**(6): p. 831.

26. Kumar, S., S. Karthikeyan, and A.F. Lee, *g-C3N4-Based Nanomaterials for Visible Light-Driven Photocatalysis.* Catalysts, 2018. **8**(2): p. 74.

27. Zhang, C., J. Liu, X. Huang, D. Chen, and S. Xu, *Multistage polymerization design for g-C3N4 nanosheets with enhanced photocatalytic activity by modifying the polymerization process of melamine.* ACS omega, 2019. **4**(17): p. 17148-17159.

28. Li, Y., M. Yang, Y. Xing, X. Liu, Y. Yang, X. Wang, and S. Song, *Preparation of Carbon‐Rich g‐C3N4 Nanosheets with Enhanced Visible Light Utilization for Efficient Photocatalytic Hydrogen Production.* Small, 2017. **13**(33): p. 1701552.

29. Zhang, M., Y. Yang, X. An, J. Zhao, Y. Bao, and L.-a. Hou, *Exfoliation method matters: The microstructure-dependent photoactivity of g-C3N4 nanosheets for water purification.* Journal of Hazardous Materials, 2022. **424**: p. 127424.

30. Zhou, Y., W. Lv, B. Zhu, F. Tong, J. Pan, J. Bai, Q. Zhou, and H. Qin, *Template-free one-step synthesis of g-C3N4 nanosheets with simultaneous porous network and S-doping for remarkable visible-light-driven hydrogen evolution.* ACS Sustainable Chemistry & Engineering, 2019. **7**(6): p. 5801-5807.

31. Subramanian, V., E.E. Wolf, and P.V. Kamat, *Catalysis with TiO2/gold nanocomposites. Effect of metal particle size on the Fermi level equilibration.* Journal of the American Chemical Society, 2004. **126**(15): p. 4943-4950.

32.   Gupta, S., M.K. Patel, A. Miotello, and N. Patel, *Metal boride‐based catalysts for electrochemical water‐splitting: a review.* Advanced Functional Materials, 2020. **30**(1): p. 1906481.

33.   Li, L., Z. Deng, L. Yu, Z. Lin, W. Wang, and G. Yang, *Amorphous transitional metal borides as substitutes for Pt cocatalysts for photocatalytic water splitting.* Nano Energy, 2016. **27**: p. 103-113.

34.   Sukanya, R. and S.-M. Chen, *Amorphous cobalt boride nanosheets anchored surface-functionalized carbon nanofiber: An bifunctional and efficient catalyst for electrochemical sensing and oxygen evolution reaction.* Journal of Colloid and Interface Science, 2020. **580**: p. 318-331.

35.   Delgado-Brito, A., D. López-Suero, A. Ruiz-Ríos, R. García-León, J. Martínez-Trinidad, J. Oseguera-Peña, and I. Campos-Silva, *Effect of the diffusion annealing process in the indentation properties of cobalt boride layer.* Ceramics International, 2019. **45**(6): p. 7767-7777.

36.   Guo, H., C.-G. Niu, Y.-Y. Yang, C. Liang, H.-Y. Niu, H.-Y. Liu, L. Li, and N. Tang, *Interfacial Co-N bond bridged CoB/g-C3N4 Schottky junction with modulated charge transfer dynamics for highly efficient photocatalytic Staphylococcus aureus inactivation.* Chemical Engineering Journal, 2021. **422**: p. 130029.

37.   Schneider, J. and D.W. Bahnemann, *Undesired role of sacrificial reagents in photocatalysis.* 2013, ACS Publications. p. 3479-3483.

38.   Kumaravel, V., M.D. Imam, A. Badreldin, R.K. Chava, J.Y. Do, M. Kang, and A. Abdel-Wahab, *Photocatalytic hydrogen production: role of sacrificial reagents on the activity of oxide, carbon, and sulfide catalysts.* Catalysts, 2019. **9**(3): p. 276.

39.   Wang, L., X. Geng, L. Zhang, Z. Liu, H. Wang, and Z. Bian, *Effects of various alcohol sacrificial agents on hydrogen evolution based on CoS2@SCN nanomaterials and its mechanism.* Chemosphere, 2022. **286**: p. 131558.

40.   Zhou, X., Y. Li, Y. Xing, J. Li, and X. Jiang, *Effects of the preparation method of Pt/gC 3 N 4 photocatalysts on their efficiency for visible-light hydrogen production.* Dalton Transactions, 2019. **48**(40): p. 15068-15073.

41.   Li, C., Y. Du, D. Wang, S. Yin, W. Tu, Z. Chen, M. Kraft, G. Chen, and R. Xu, *Unique*

P☐Co☐N Surface Bonding States Constructed on g‑C3N4 Nanosheets for Drastically Enhanced Photocatalytic Activity of H2 Evolution. Advanced Functional Materials, 2017. **27**(4): p. 1604328.

42.   Gouget, G., D.P. Debecker, A. Kim, G. Olivieri, J.-J. Gallet, F. Bournel, C. Thomas, O. Ersen, S. Moldovan, and C. Sanchez, *In situ solid–gas reactivity of nanoscaled metal borides from molten salt synthesis.* Inorganic Chemistry, 2017. **56**(15): p. 9225-9234.

43.   Bagus, P.S., E.S. Ilton, and C.J. Nelin, *The interpretation of XPS spectra: Insights into materials properties.* Surface Science Reports, 2013. **68**(2): p. 273-304.

44.   Brédas, J. and A. Heeger, *Influence of donor and acceptor substituents on the electronic characteristics of poly (paraphenylene vinylene) and poly (paraphenylene).* Chemical physics letters, 1994. **217**(5-6): p. 507-512.

45.   Kampouris, D.K., X. Ji, E.P. Randviir, and C.E. Banks, *A new approach for the improved interpretation of capacitance measurements for materials utilised in energy storage.* Rsc Advances, 2015. **5**(17): p. 12782-12791.

จุฬาลงกรณ์มหาวิทยาลัย
CHULALONGKORN UNIVERSITY

VITA

NAME	ชยธร ประไพตระกูล
DATE OF BIRTH	9 กุมภาพันธ์ 2540
PLACE OF BIRTH	กรุงเทพฯ
INSTITUTIONS ATTENDED	Bachelor's degree: Nanotechnology Engineering of Chulalongkorn University
	Master's degree: Chemical Engineering of Chulalongkorn University and National Taiwan University
HOME ADDRESS	87/70 หมู่บ้านลดาวัลย์, ถนนราชพฤกษ์, แขวงบางแวก, เขตภาษีเจริญ, กรุงเทพ 10160